# TAC-C uncovers open chromatin interaction in crops and SPL-mediated photosynthesis regulation

Jingmin Kang[1,2,#], Zhaoheng Zhang[1,3,#], Xuelei Lin[1,#], Fuyan Liu[2,#], Yali Song[2,#], Peng Zhao[1,4], Yujing Lin[1], Xumei Luo[1,3], Xiaoyi Li[5], Yanyan Li[5], Wenda Wang[5], Cuimin Liu[1], Shengbao Xu[4], Xin Liu[2], Jun Xiao[1,3,6,*]

[1]Institute of Genetics and Developmental Biology, Chinese Academy of Sciences, Beijing 100101, China

[2]BGI Research, Beijing 102601, China

[3]University of Chinese Academy of Sciences, Beijing 100049, China

[4]College of Agronomy, Northwest A&F University, Yangling, Shaanxi 712100, China

[5]Institute of Botany, Chinese Academy of Sciences, Beijing 100093, China

[6]Centre of Excellence for Plant and Microbial Science (CEPAMS), JIC-CAS, Beijing 100101, China

[#]Equal contributions: Jingmin Kang, Zhaoheng Zhang, Xuelei Lin, Fuyan Liu, Yali Song

[*]Corresponding author. Email: jxiao@genetics.ac.cn

**Abstract**

*Cis*-regulatory elements (CREs) direct precise gene expression for development and environmental response, yet their spatial organization in crops is largely unknown. We introduce Transposase-Accessible Chromosome Conformation Capture (TAC-C), a method integrating ATAC-seq and Hi-C to capture fine-scale chromatin interactions in four major crops: rice, sorghum, maize, and wheat. TAC-C reveals that chromatin interaction frequency aligns with genome size and gene expression, exhibiting distinct loop structures between C3 and C4 plants, particularly in C4-specific enzymes coding genes. Integrating chromatin structure with population genetics data highlights that chromatin loops connect distal regulatory elements to phenotypic variation. Asymmetrical open chromatin interactions among subgenomes, driven by transposon insertions and sequence variations, contribute to biased homoeolog expression. Furthermore, TaSPL7/15 regulate photosynthesis-related genes through chromatin interactions, with enhanced photosynthetic efficiency and starch content in *Taspl7&15* mutant. TAC-C provides new insights into the spatial organization of regulatory elements in crops, especially for SPL-mediated photosynthesis regulation in wheat.

**Key words:** TAC-C Reveals Chromatin Interactions and SPL-Mediated Photosynthesis Regulation in Crops.

## Introduction

*Cis*-regulatory elements (CREs) are crucial for fine-tuning gene expression, influencing phenotypic diversity, and accelerating crop improvement (*1-4*). In rice, a 5.3 kb silencer upstream of the spike development gene *FRIZZY PANICLE* (*FZP*) is bound by Brassinazole 1 (*OsBZR1*), suppressing *FZP* expression and influencing spike architecture and yield (*5*). In maize, a distal region over 40 kb upstream of *TEOSINTE BRANCHED1* (*TB1*) act in *cis* to alter *TB1* transcription, impacting inflorescence structure (*6*). In sorghum, binding by WRKY and ZF-D (zinc finger-DHHC) transcription factors (TFs) activates the aluminum tolerance gene *multidrug and toxic compound extrusion* (*SbMATE*), enhancing tolerance (*7*). These active CREs are typically located in accessible chromatin regions (ACRs) and can act as proximal or distal elements, influencing gene expression locally or over long distances (*8*). Techniques such as Assay for Transposase Accessible Chromatin sequencing (ATAC-seq), DNase-seq, and Formaldehyde-Assisted Isolation of Regulatory Elements (FAIRE-seq) have effectively identified ACRs across plant genomes, though they do not capture their spatial organization (*9-11*). The number of ACRs correlates with gene density, and in larger genomes, distal ACRs—often functioning as enhancers—are abundant (*12*). These distal elements play a key role in regulating tissue-specific gene expression, particularly in species with large genomes (*13*).

Recent advancements, including Chromosome conformation capture (3C) coupled with sequencing (Hi-C), Chromatin interaction analysis by paired-end tag sequencing (ChIA-PET), *in situ* Hi-C followed by chromatin immunoprecipitation (HiChIP), open chromatin enrichment and network Hi-C (OCEAN-C), and chromatin interaction analysis by ATAC (ChIATAC), have significantly enhanced our understanding of chromatin interactions and three dimensional (3D) genome structures (*14-18*). The dynamics of chromatin loops are crucial for regulating organ development and stress responses in crops (*19, 20*). The structure of chromatin provides a physical framework for gene regulation, by reducing the physical distance between *cis*-regulatory elements and target genes, chromatin organization provides a framework for efficient gene regulation, especially in large genome like maize and wheat, where nuclear metabolic efficiency is vital (*21, 22*).

Polyploidy, common in crops (*23*), often leads to chromatin structure distinct from those in diploid species, with inter-subgenome chromatin interactions forming a novel regulatory layer that supports coordinated gene expression (*24, 25*). While Hi-C provides a broad view of genome-wide interactions, it may overlook critical contacts between open chromatin and distal regulatory elements (*26*). Techniques like ChIA-PET and HiChIP offer more specificity, focusing on interactions mediated by DNA-binding proteins or histone marks (*14, 17*). OCEAN-C integrates Hi-C with FAIRE-seq but lacks the signal clarity and TFs binding footprint resolution of ATAC-seq (*27, 28*). ChIATAC employs Sodium dodecyl sulfate (SDS) treatment of nuclei, producing data distinct from ATAC-seq (*18*). There remains a need for methods that better capture the spatial organization of open chromatin to deepen our understanding of long-range transcriptional regulation.

Common wheat (*Triticum aestivum*, *T. aestivum*) is a widely cultivated allohexaploid crop with a complex genome structure due to its polyploidization, comprising three subgenomes (A, B, and D) and a total genome size of 16G (*29*). This makes wheat an ideal model for exploring the 3D spatial organization of large-genome species. Studies using Hi-C and HiChIP have revealed that interactions within subgenomes are more

frequent than those between subgenomes (*30*), indicating a higher-order organization favoring subgenome-specific affinities. ATAC-seq has identified numerous CREs in wheat that play vital roles in gene expression and phenotypic traits (*4, 31, 32*). However, the mechanisms by which distal CREs, particularly their long-range interactions, regulate gene expression remain poorly understood. High-resolution open chromatin interaction maps generated using OCEAN-C for wheat and its tetraploid and diploid relatives reveal more frequent chromatin interactions within the D subgenome (*28*), suggesting that it may have evolved more rapidly and retained more epigenetic features from its diploid ancestors. Despite advancements, critical questions remain, such as how specific quantitative trait locus (QTLs) and expression quantitative trait locus (eQTLs) regulate gene expression through long-range interactions, the role of chromatin interactions in homoeolog gene expression bias, and the mechanisms driving chromatin loop formation in wheat.

The establishment and maintenance of nuclear 3D structures have long posed challenges in 3D genome research (*33, 34*). In animals, the chromatin loop formation is often mediated by CCCTC-binding factor (CTCF) and cohesin complexes (*35-37*). The TF Zinc Finger Protein 143 (ZNF143) in animals has been shown to work in tandem with CTCF, regulating CTCF/cohesin interactions and influencing topologically associating domains (TADs) formation (*38*). The lack of a CTCF homolog in plants suggests that any TAD-like structures observed in plants may have evolved through independent pathways (*39*). Recent studies have indicated that in rice (*39*), members of the TCP (Teosinte branched1/Cycloidea/Proliferating cell factor) family of TFs may play a role similar to CTCF in animals. TCPs have been found to recognize specific motifs at the boundaries of rice TAD-like structures (*39*). Additionally, TCP TF activity has been linked to 3D chromatin structure regulation in the liverwort *Marchantia* (*40*). Despite these advances, research into TFs mediating 3D genome structures in wheat remains limited. Investigating the role of specific wheat TFs in nuclear architecture could provide valuable insights into plant genome regulation and evolutionary parallels between plant and animal 3D genome structures.

In this study, we developed the Transposase-Accessible Chromosome Conformation Capture (TAC-C) technique, integrating *in situ* Hi-C and ATAC-seq to map fine-scale open chromatin interactions in wheat, rice, maize and sorghum. We explored the regulatory effects of distal open chromatin on gene expression, focusing on asymmetrical open chromatin interactions within different wheat subgenomes. Additionally, we uncovered the key role of SBP (SQUAMOSA promoter binding protein) family TFs in shaping chromatin interactions and their significant impact on regulating photosynthetic energy metabolism in wheat. These findings provide valuable insights and resources for studying 3D genome architecture and transcriptional regulation in complex crop genomes.

## Results

### TAC-C efficiently capture fine-scale chromatin interactions

To capture chromatin interactions at accessible regions and explore long-range transcriptional regulatory processes in large-genome species with low sequencing depths, we developed a new strategy. This method integrates ATAC-seq with Hi-C, resulting in a more efficient technique we term Transposase-Accessible Chromosome Conformation Capture (TAC-C). Plant tissue was first fixed with formaldehyde, followed by the extraction of high-quality nuclei. To preserve open chromatin regions,

we avoid SDS treatment and instead perform *in situ* restriction enzyme digestion with DpnII, followed by biotin labeling and proximity ligation, slightly differing from traditional *in situ* Hi-C protocol. Next, we apply transposase for *in situ* tagmentation, as per the ATAC-seq protocol. Biotin-labeled chromatin ligation products are isolated using biotin-streptavidin affinity, and the TAC-C library is generated through PCR (**Fig. 1A**, see Methods for details).

The TAC-C data exhibited high reproducibility between biological replicates (**fig. S1A, table S1**). The TAC-C interaction map at the chromosome level exhibited robust signals along the primary diagonals and anti-diagonal lines (**Fig. 1B and fig. S1B**). This pattern reflected the Rabl-like chromosome configuration, consistent with the Hi-C interaction matrices as reported (*30*), indicating that TAC-C data can effectively depict the high-order organization of the wheat genome. We then evaluated the effect of sequencing depth on the TAC-C peak calling and compared it against OCEAN-C and ATAC-seq techniques (*16, 41*). As the read count increased, TAC-C generated peaks similar to or even more than ATAC-seq, largely outperforming OCEAN-C (**Fig. 1C**), suggesting that TAC-C more effectively capture open chromatin regions.

In wheat, we identified 332,927 overlapping TAC-C peaks from two biological replicate libraries (Rep1: 398 million reads; Rep2: 405 million reads) for subsequent analysis. These peaks were categorized as gene body (g, 36.7%), promoter (p, 33.7%), and distal (d, 29.6%) CREs (**Fig. 1D**). TAC-C and ATAC-seq peaks were strongly enriched at transcription start sites (TSS), largely more than OCEAN-C peaks (**Fig. 1E**). Correlation analysis with epigenetic markers revealed that TAC-C peaks are predominantly associated with active histone modifications (H3K4me3, H3K9ac, and H3K27ac), similar to ATAC-seq and remarkably higher than OCEAN-C and Hi-C peaks (*30, 41*) (**Fig. 1F**). This indicates that TAC-C peaks are mostly located in active *cis*-acting elements, such as promoters or enhancers. We further compared TAC-C with OCEAN-C and Hi-C in identifying open chromatin interactions. TAC-C identified 159,667 intrachromosomal loops (**table S2**), classified into proximal anchors (P) within 3 kb distance to TSS of genes and distal anchors (D) beyond 3 kb. The loops consisted of 55.5% P-P interactions (PPIs), 35.5% P-D interactions (PDIs), and 9.0% D-D interactions (DDIs) (**Fig. 1G**). TAC-C showed a higher proportion of P-P interaction and detected shorter loop spans compared to OCEAN-C and Hi-C (**Fig. 1H**), indicating TAC-C's superior performance in detecting fine-scale open chromatin interactions (**Fig. 1I**). Furthermore, we observed more frequent interactions between chromosomes within the same subgenome consistenting with previous studies (*25*), while no significant differences in intrachromosomal interaction frequencies were detected between A, B and D subgenomes.

In summary, we have developed the TAC-C assay by integrating *in situ* Hi-C and ATAC-seq protocols, validating it experimentally in bread wheat. This method enhances the ability to capture open chromatin interactions, particularly in large-genome crops like wheat.

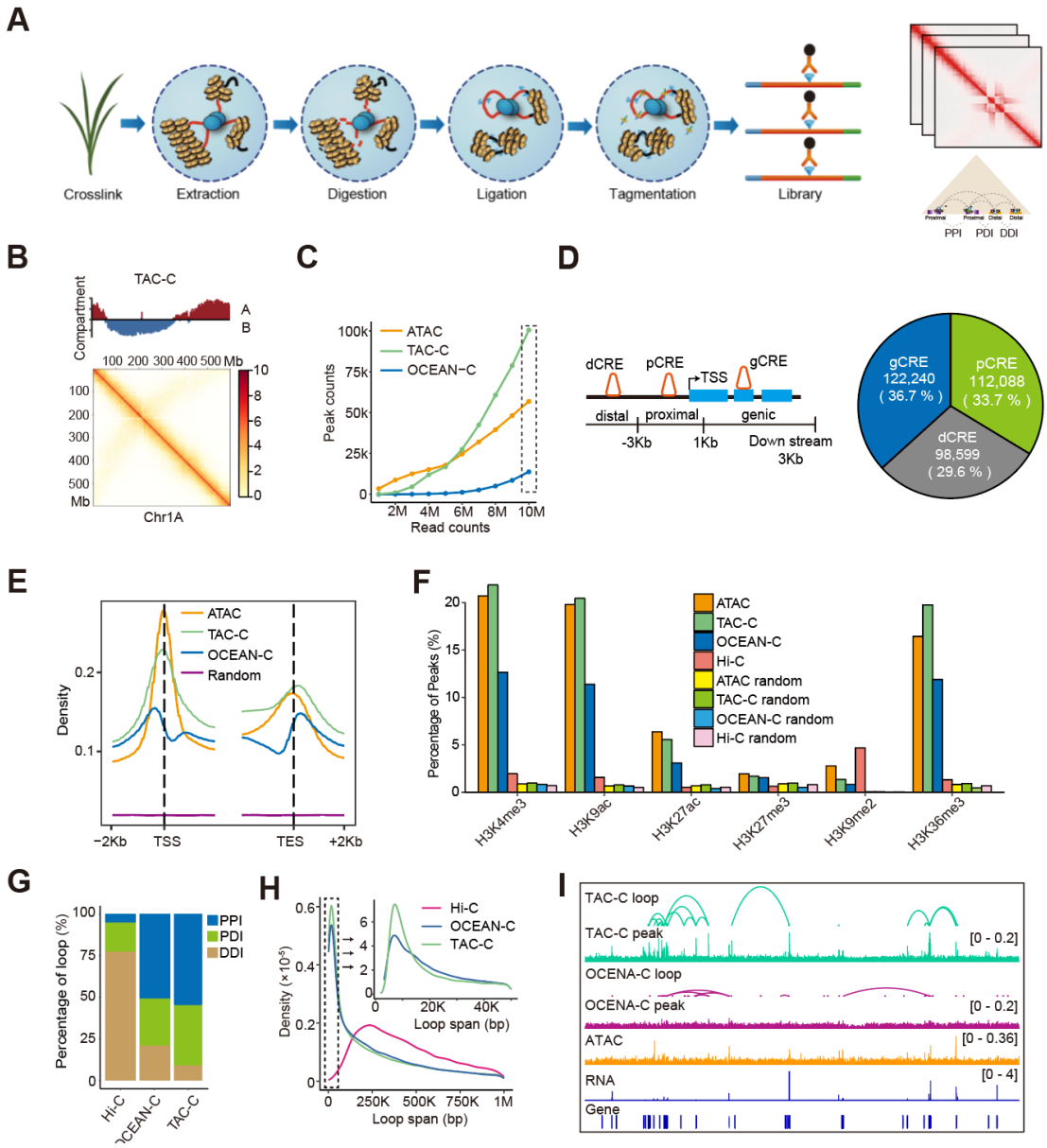


**Fig. 1 Identification of open chromatin interactions using TAC-C and comparison with other techniques**

**A.** Schematic of TAC-C.

**B.** TAC-C interaction matrix at 1Mb resolution across chromosome 1A, with chromatin compartments shown as a track above the contact map. Compartment A is marked in red, and compartment B in blue.

**C.** Statistical comparison of peak capture efficiency under different sequencing depth using TAC-C, ATAC, and OCEAN-C.

**D.** Classification of CREs based on their distribution around genes, with the number and proportion of each CRE type of CRE indicated. TSS: transcription start site, dCRE: distal CRE, pCRE: proximal CRE, gCRE: genic CRE.

**E.** Density plot of TAC-C, OCEAN-C, ATAC, and random regions around transcription start site (TSS) and transcription termination site (TTS).

**F.** Percentage overlap of TAC-C, OCEAN-C, Hi-C, and ATAC peaks or random regions with various histone modification marks.

**G.** Percentage of proximal-proximal interactions (PPI), proximal-distal interactions

(PDI), and distal-distal interactions (DDI) identified by TAC-C, OCEAN-C and Hi-C. **H.** Loop span distribution of open chromatin interactions identified by TAC-C, OCEAN-C and Hi-C. Regions with loop span below 50kb are highlighted in the top right corner.
**I.** Example of open chromatin interactions: browser view of a 6.6Mb region showing a randomly selected open chromatin interactions with associated TAC-C and OCEAN-C data.

**Conserved and distinct features of chromatin interactions across four crop species**

To explore the characteristics of interacted open chromatins in crops, we also conducted TAC-C experiments on young leaves from Rice (*Oryza. Sativa*, *O. sativa*), Sorghum (*Sorghum. Bicolor*, *S. bicolor*) and Maize (*Zea. Mays*, *Z. mays*) (**fig. S1A, S1E and S1F**). The results demonstrated high reproducibility between biological replicates, with high-quality contact matrices and enriched TAC-C signals around TSS and TES. The number of identified loops ranged from 46,327 to 159,667 across species, with species with larger genomes having more loops identified (**Fig. 2A and fig. S2A**). Larger genomes (*Z. mays* and *T. aestivum*) displayed notably longer distances for open chromatin interactions compared to smaller genomes (*O. sativa* and *S. bicolor*), with a greater percentage of PDI and DDI (**Fig. 2B and fig. S2B-C**).

Chromatin loops have been implicated in gene expression regulation (*42, 43*). We found that gene pairs looped together tended to exhibit high expression levels simultaneously (**fig. S2D**). Genes were further divided into four levels based on chromatin interaction frequencies ranked from low to high (L1: 0-25%; L2:25-50%; L3:50-75%; L4:75-100%), Across all four species, gene with more interactions showed higher expression levels (**Fig. 2C and fig. S2E**), suggesting a positive correlation between chromatin interaction frequencies and gene expression. The top 10% most frequently interacting anchors were defined as “hub anchors”, their partners as “connecting anchors”, whereas, other open chromatin peaks that were not located in the loop anchor were defined as basal peaks. Hub anchor-linked genes termed as “node genes” and connecting anchor-linked genes as “connecting genes” (*44*) (**Fig. 2D and fig. S2F**). Hub anchors exhibited higher TAC-C signals (**Fig. 2E**), while node genes shown lower SNP densities and higher expression levels across all four species (*45-48*) (**Fig. 2F and 2G**). Furthermore, node genes exhibited the highest proportion of orthologous genes across the four species, followed by connect genes (**Fig. 2H**). Overall, these results highlight the conservation and importance of hub anchors and node genes.

Taken together, the span and number of open chromatin interactions were influenced by genome size and gene count across species, with interaction frequency significantly influencing gene expression. Hub anchors display higher TAC-C signals, while node genes exhibit elevated expression levels and conserved sequences, indicating their significant biological roles.

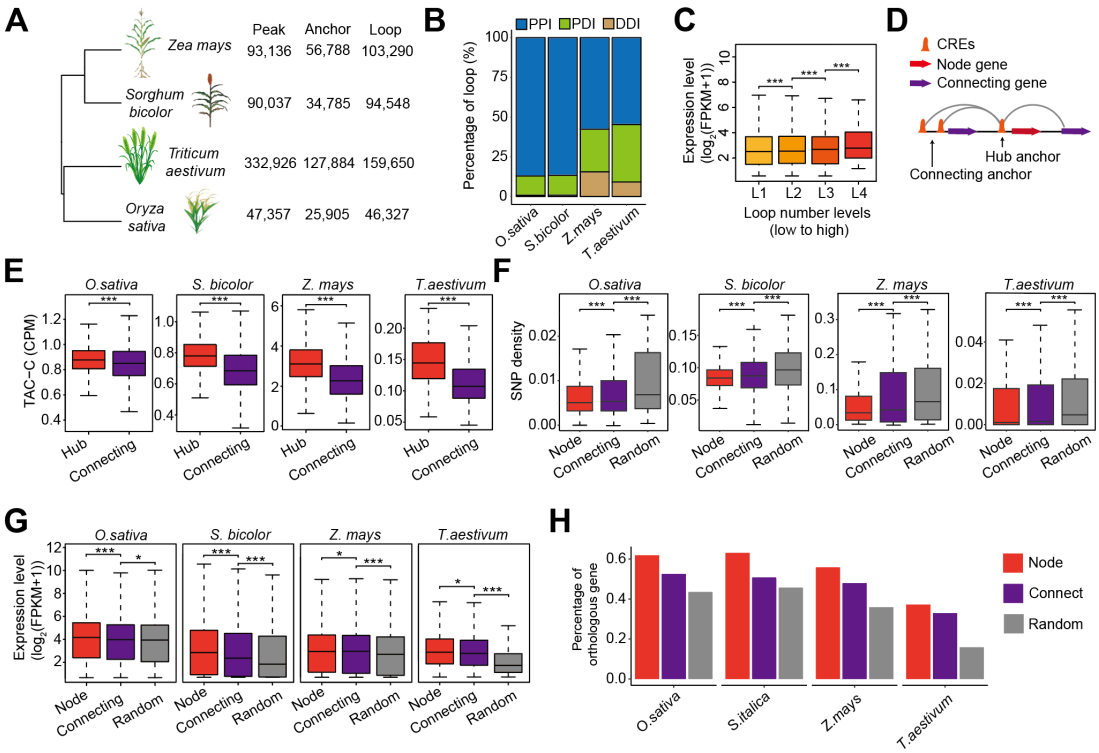


**Fig. 2 Characteristics of chromatin interactions across four crops species**

**A.** Phylogenetic tree of four crop species with the number of peaks, anchors, and loops identified from TAC-C data.
**B.** Percentage distribution of PPI, PDI, and DDI across the four crop species.
**C.** Expression levels ($\log_2$(FPKM+1)) of genes with varying levels of chromatin interactions in *T. aestivum*. ***, $p$<0.001 from Student's $t$-test.
**D.** Schematic representation of the hub-and-connection anchor model of chromatin interactions, with definitions of for node and connecting genes based on contact frequency.
**E.** TAC-C signal intensity in hub and connecting anchor regions across the four crop species. ***, $p$<0.001 from Student's $t$-test.
**F-G.** SNP density (**F**) and expression levels (**G**) in node, connecting and random genes across the four crop species. *, $p$<0.05, **, $p$<0.01, ***, $p$<0.001 from Student's $t$-test.
**H.** Percentage of orthologous genes in node, connect and random genes in four crops. The information of gene orthologous relationship across the four species was obtained from TGT (http://wheat.cau.edu.cn/TGT/).

## Chromatin interaction link regulatory elements to phenotype variation in wheat

To explore the importance of spatial organization of chromatin, we compiled data from published sources on QTLs and eQTLs related to various agronomic traits (**table S3**), as well as breeding selection sweeps (SS) in wheat to investigate whether chromatin interactions could spatially link distal regulatory elements to target genes, ultimately contributing to phenotypic variation (*50-53*). Our analysis revealed that hub anchors, which primarily localize to the distal ends of chromosomes, showed a distribution pattern consistent with "functional regions" as defined by QTLs, eQTLs and SS (**Fig. 3A**). Notably, hub anchors exhibited the highest overlap with these functional regions, followed by connecting anchors and basal peaks (**Fig. 3B**), suggesting that regions frequently involved in chromatin loops may play more crucial roles in gene regulation. Furthermore, QTLs overlapped with the hub anchor exhibit stronger significance, while

262 eQTLs and genes looped by the hub anchor demonstrate larger effect sizes (*51, 54*)
263 (**Fig. 3C and 3D**). Furthermore, activating histone modifications (H3K4me3,
264 H3K27ac) are enriched in QTL regions associated with loops, whereas the repressive
265 histone mark H3K9me3 shows no significant differences among groups (**fig S3**). This
266 further supports that these regions may function as enhancer. Interestingly, the
267 H3K27me3 modification is also slightly enriched, although no distinct peaks are
268 observed. These regions may indicate the bivalent enhancer.

269 In total, 7,632 hub anchors overlapped QTLs, eQTLs and breeding selection sweeps.
270 Of these, only 259 hub anchors were common across all three regions (**Fig. 3E**). For
271 instance, an eQTL (Chr5A_645725) located 621 kb downstream of the leaf width-
272 regulated gene *NARROW LEAF1* (*TaNAL1-like-5A*) was found within a flag leaf area
273 (FLA)-regulated QTL and a breeding selection region (*51, 55, 56*). This eQTL, located
274 in a hub anchor, was observed to loop with *TaNAL1-like-5A* (**Fig. 3F**). Furthermore, the
275 functional potential of these distal regulatory regions was established through a
276 luciferase reporter assay. *TaNAL1-like-5A* carrying the distal regions exhibited robust
277 activity in the reporter assay, with higher signals compared with the controls carrying
278 the 35S promoter alone (**Fig. 3G**). These findings suggest that distal regulatory
279 elements can modulate target gene expression through chromatin interactions, thereby
280 influencing phenotypic variation. To explore the genetic variation underlying this
281 regulation, haplotype analysis was conducted for both *TaNAL1-like-5A* and the distal
282 eQTL region Chr5A_645725 (*57*) (**Fig. 3F**). This analysis identified three distinct
283 haplotypes, each exhibiting significant differences in flag leaf length, width and flag
284 leaf area across various natural populations (*57*) (**Fig. 3H**).

285 Our findings reveal that distal elements may regulate the expression of target genes
286 through chromatin interactions, thereby influencing phenotypic variation. Providing
287 physical topological information support for distal regulatory sites identified through
288 Genome-Wide Association Studies (GWAS) and Transcriptome-Wide Association
289 Studies (TWAS).

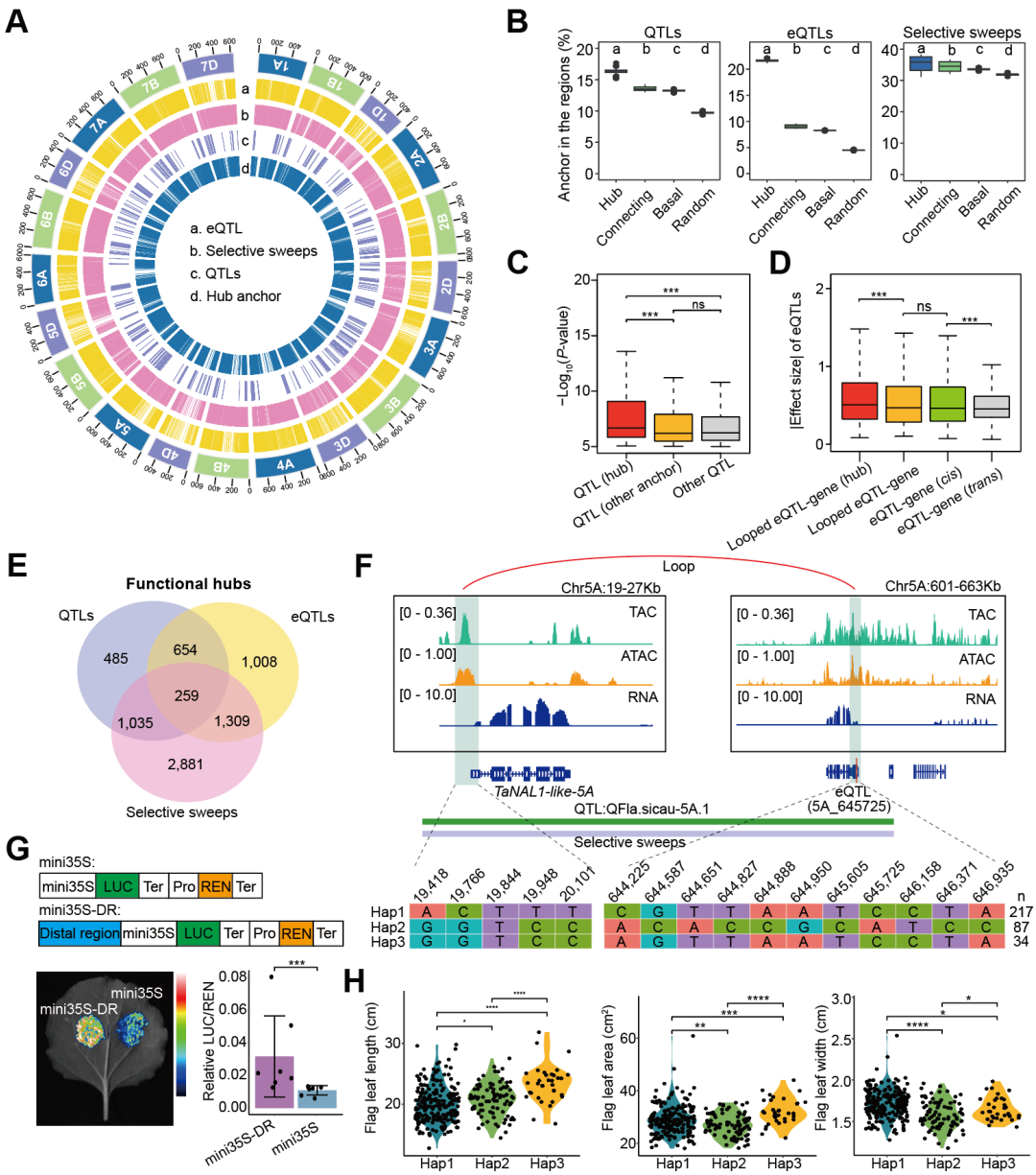


**Fig. 3 Long-range chromatin interactions regulate gene expression and associate with trait variations**

**A.** Circos plot showing the distribution of wheat eQTLs (a), breeding selective sweeps (b), QTLs (c), and hub anchors (d) across the wheat genome.

**B.** Percentage of overlapping interactions between hub anchors, connecting basal anchors, and random regions with QTLs, eQTLs and breeding selective sweep. To reduce false positives, 1000 permutation tests were conducted. In each test, 60% of accessions were randomly sampled, and differences were calculated using least significant difference (LSD) test.

**C.** Significance of GWAS signals for SNPs located in hub anchor, other anchors and QTL regions. GWAS signals data were obtained from published sources (details in table S3). ***, $p<0.001$, ns, $p>0.05$ from Student's *t*-test.

**D.** Absolute effect size of looped eQTL-gene pairs compared to other eQTL-gene pair. Looped eQTL-gene (hub) pairs refer to those where the eQTL is located in the anchors or hub anchors. Effect size data were sourced from published studies (details in table S3). ***, $p<0.001$, ns, $p>0.05$ from Student's *t*-test.

**E.** Venn diagram showing the overlap between hub anchors, QTLs, eQTLs, and breeding selective sweeps.
**F.** Open chromatin loop between *TaNAL1-like-5A* and distal eQTL (5A_645725). Green and pink tracks indicate QTL and breeding selection sweeps regions. The table below shows haplotypes of SNP sites in *TaNAL1-like-5A* and the distal regulatory region.
**G.** Luciferase reporter assays validating the transcriptional regulatory role of the distal region on *TaNAL1-like-5A*. The distal anchor sequences, containing the eQTL locus, was introduced into the proximal region of *TaNAL1-like-5A* promoter (Distal region). ***, $p \leq 0.001$ from Student's *t*-test.
**H.** Comparison of flag leaf length, width and leaf area of *TaNAL1-like-5A* in three haplotypes of the loop- linked *TaNAL1-like-5A* and eQTL (5A_645725). *, $p \leq 0.05$; **, $p \leq 0.01$; ***, $p \leq 0.001$; ****, $p \leq 0.0001$ from Student's *t*-test.

**Asymmetric chromatin interaction associates with homoeolog expression bias in wheat**

Since wheat is a hexaploid species, with proportion of A, B, and D subgenomes showing imbalanced expression pattern (*58*), we wonder whether differences in chromatin interactions among subgenomes contribute to this expression bias. We compared the loops at subgenomic levels for each chromosome. Interestingly, while the strength of the loops was comparable across three subgenomes, the D subgenome exhibited significantly more loops than the A and B subgenomes, consistent with previous study (*28*) (**fig. S4A, B**). In total, 39,714, 36,643, and 41,559 PPIs were identified in A, B, and D subgenomes, respectively. Among these, 3,742, 5,337 and 5,257 PPIs were conserved between two AB, AD and BD subgenomes, respectively. And 7,504 PPIs were conserved across all three subgenomes (**Fig. 4A**), indicating asymmetrical interactions between subgenome.

The coverage of transposable elements (TEs) in singleton loops was significantly higher than in homoeolog PPIs across subgenomes, suggesting a link between transposon insertion and the occurrence of asymmetrical interactions (**Fig. 4B**). The loop strength for ABD-conserved PPIs was the highest, while singleton PPIs exhibited the weakest loop strength (**Fig. 4C**). Additionally, 56.7% of loop anchors for ABD-conserved PPIs were classified as hub anchors, indicating that ABD-homoeolog interactions may represent crucial regulatory regions (**Fig. 4D**). Furthermore, homoeolog PPIs demonstrated a higher overlap with functional regions (**Fig. 4E**), and GO enrichment analysis revealed that genes associated with conserved PPIs are primarily involved in carbohydrate metabolism, photosynthesis, and growth and development (**fig. S4C**). In contrast, genes located in singleton loops were mainly enriched in basic cellular processes (**fig. S4D**).

To assess whether asymmetrical PPIs influence homoeolog expression bias, we compared the expression level of 16,539 triads containing at least one homoeolog linked with a loop. As expected, there were no significant differences in expression for ABD-conserved PPI-linked homoeologs. However, for PPIs conserved in only two subgenomes (AB, AD and BD), the expression levels of homoeolog lacking loops were significantly lower than the other two homoeologs (**Fig. 4F**). Furthermore, the proportion of balanced expression triads was highest in ABD-conserved PPI-linked genes. Homoeolog lacking loops were more likely to be suppressed in AB-, AD- or BD-conserved PPIs (**Fig. 4G**), indicating that asymmetrical interactions may be an important regulatory factor influencing homoeolog expression bias.

To explore the relationship between epigenetic modifications and asymmetrical PPIs,

we analyzed histone modifications in the 5 kb regions flanking the asymmetrical loop-linked homoeolog triads. Activation histone marks, specifically H3K36me3 and H3K9ac, were correlated with the levels of PPI asymmetry. Homoeolog lacking loops exhibited lower coverage of these histone marks (**Fig. 4H**). Conversely, other epigenetic signals (ATAC, H3K27ac, H3K4me3, and H3K27me3) did not show significant difference (**fig. S4E**). For instance, a homoeolog triad (*TraesCS1A03G0004300*, *TraesCS1B03G0002100*, and *TraesCS1D03G0000500*) looped with another homoeolog triad (*TraesCS1A03G0005200*, *TraesCS1B03G0003300* and *TraesCS1D03G0001500*) in B and D subgenomes, but this interaction was absent in the A subgenome (**Fig. 4I**). These asymmetrical loops were associated with elevated expression levels and activating chromatin modification signals in the B and D subgenomic homoeologs.

To further understand the factors driving asymmetrical PPIs, we compared TE coverage and sequence similarity in the 5 kb regions flanking the asymmetrical loop-linked homologous triads (**Fig. 4J and 4K**). The results showed that homoeolog lacking loops exhibited higher TE coverage and lower sequence similarity in their flanking regions. This suggests that transposon insertion or sequence variation may disrupt loop structure, leading to the loss of homologous loops in specific subgenomes.

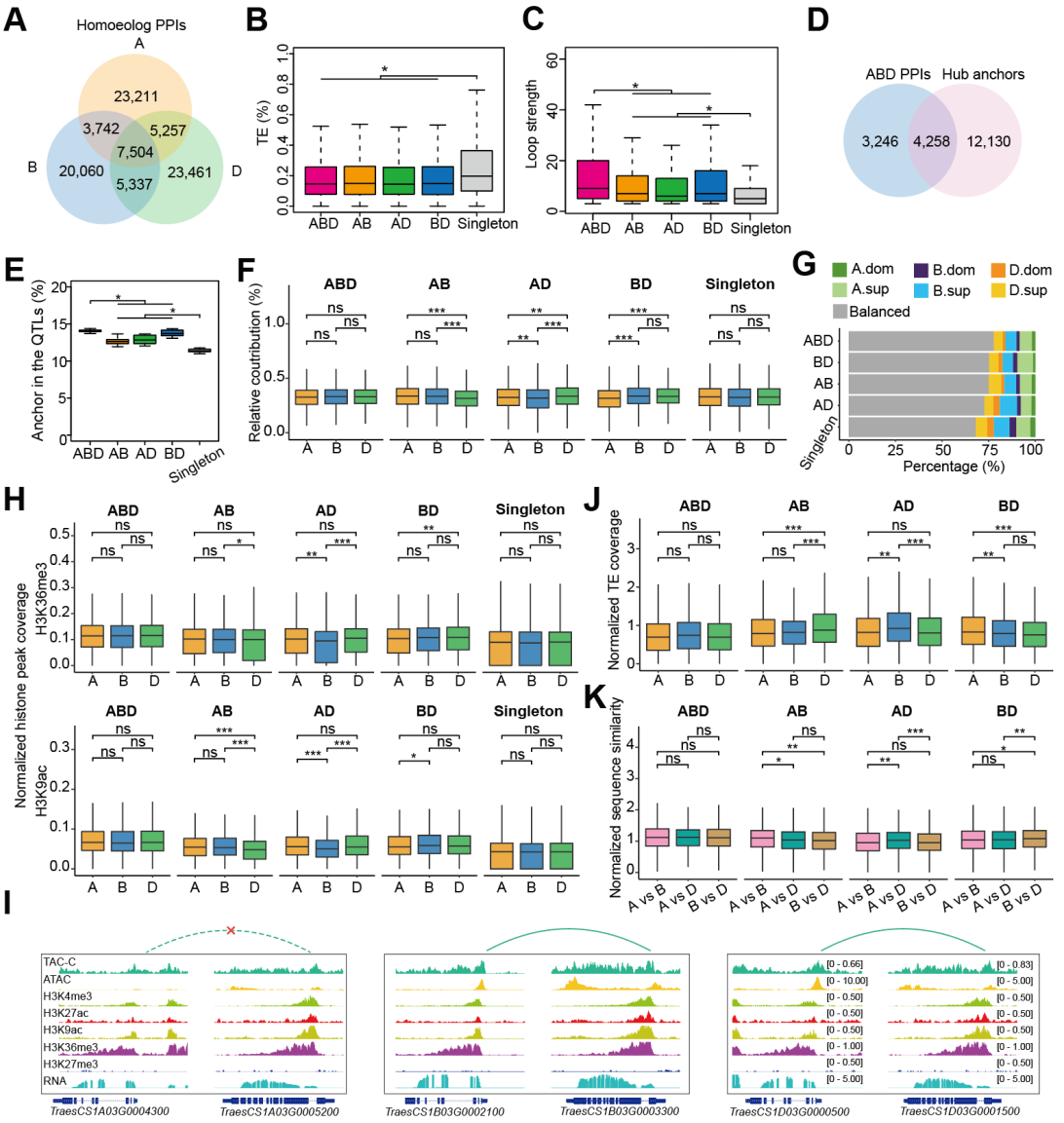

**Fig. 4 Asymmetrical open chromatin loops associated with homoeolog expression bias, epigenetic profiling, TE insertions, and sequence variations**

**A.** Venn diagram showing the overlap of homoeolog PPIs between the A, B, and D subgenomes.
**B-C.** Boxplots illustrating the TE coverage (**B**) and loop strength (**C**) across loop anchors at different homoeolog levels. ABD: homoeolog PPIs in all three subgenomes; AB, AD or BD: homoeolog PPIs in AB, AD or BD subgenomes; Singleton: PPIs in only one of the subgenomes A, B or D. *, $p \leq 0.05$ from Student's *t*-test.
**D.** Venn diagram showing the overlap between homoeolog ABD PPIs and hub anchors.
**E.** Overlap ratio of QTL regions with PPI anchors at different homoeolog levels, normalized by the average QTL coverage in A, B and D subgenomes, respectively.
**F.** Relative expression contribution of each subgenome based on triad, classified into five groups according to homoeolog PPI levels. *, $p \leq 0.05$; ***, $p \leq 0.001$ from Student's *t*-test.
**G.** Proportion of triads in each homoeolog expression bias category across the five homoeolog PPI groups.
**H.** Coverage of H3K36me3 (upper) and H3K9ac (bottom) peaks in gene flanking regions (±5kb) across subgenomes, normalized to subgenome averages, classified by homoeolog PPI levels. *, $p \leq 0.05$; **, $p \leq 0.01$; ***, $p \leq 0.001$ from Student's *t*-test.
**I.** Browser screenshot showing asymmetrical open chromatin interactions and expression of linked gene (*TraesCS1A03G0004300*, *TraesCS1B03G0002100*, and *TraesCS1D03G0000500*). Data tracks include TAC-C peaks, loops, histone modifications, ATAC profiling, and gene transcription.
**J.** TE coverage in gene flanking regions (±5kb) across subgenomes, normalized by the average TE coverage of singleton PPIs in A, B and D subgenomes.
**K.** Pairwise comparisons of sequence similarity in gene flanking regions (±5kb) across subgenomes, normalized by the average gene sequence similarity between A vs B, B vs D, and A vs D, classified by homoeolog PPI levels. *, $p \leq 0.05$; **, $p \leq 0.01$; ***, $p \leq 0.001$ from Student's *t*-test.

**SBP and ERF family TFs occupy chromatin interaction-linked gene regulation**

Chromatin conformation regulates transcription by looping TF bound CREs to the promoters of distally located target genes, as observed in mammalian cell (*38, 59*) (**Fig. 5A**). To explore this mechanism in plants, we analyzed the enrichment of TFs at open chromatin interaction anchors. We found that binding sites of TF from the V-myb avian myeloblastosis viral oncogene homolog (MYB), DNA binding with one finger (Dof), ethylene responsive factor (ERF), GATA and SBP families were significantly enriched within the anchor region (**Fig. 5B**), with SBP and ERF binding motif-enriched loops exhibiting stronger interactions compared to others (**Fig. 5C)**.

To assess the biological significance of these TF binding sites-enriched anchors, we examined their presence in functional hubs (the hubs overlapped with previous defined functional regions). Notably, 14.34% of the SBP family TF binding sites were localized in functional regulatory regions, higher than other TF families (**Fig. 5D**). In addition, SBP and ERF-bound functional hub anchor linked to significantly more number of target genes compared to other hub anchors, indicating the importance of SBP and ERF targets in functional regions (**Fig. 5E**). Using published DAP-seq data for SBP, ERF, MYB, and Dof TF families, we found that the SBP and ERF DAP-seq peaks were more enriched in anchor regions (*60*) (**fig. S5A**), with SBP-bound loops showing enhanced interaction strength (**fig. S5B**). This suggest that SBP and ERF TFs are closely

associated with chromatin interactions, emphasizing the importance of SBP-bound loops in transcriptional regulation.

Further analysis categorized genes based on SBP-associated chromatin interactions and occupancy (*44*) (**Fig. 5F**). Genes with SBP binding at one or both anchors (a4, a5, and a6) exhibited higher expression levels than those without SBP binding (a3) (**Fig. 5F**). However, basal genes not involved in chromatin interaction showed similar expression levels regardless of SBP binding (a1, a2), indicating that chromatin loops and SBP binding synergistically enhance transcription within chromatin loop.

In conclusion, we identified five TF family (MYB, Dof, ERF, GATA, and SBP) significantly enriched in open chromatin anchor regions, suggesting their role in the formation or functional regulation of chromatin interaction.

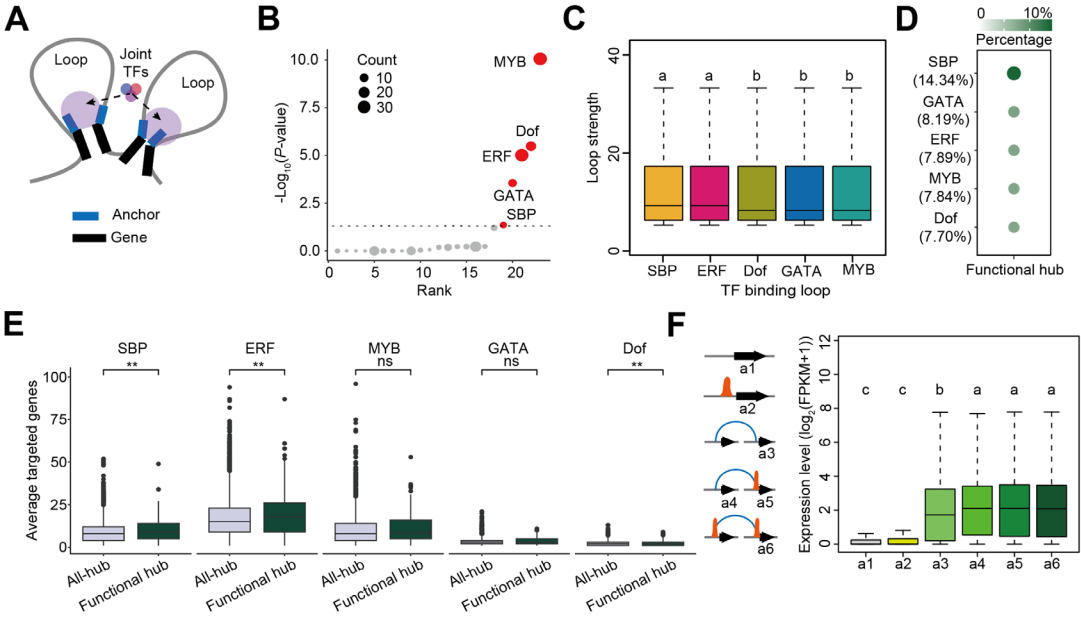


**Fig. 5 Identification of TFs enriched in the chromatin interaction regions**

**A.** Schematic diagram illustrating joint TFs binding at the anchors of open chromatin interaction.
**B.** TF family enrichment analysis in hub anchor regions (two-sided Fisher's exact test). Significantly enriched TF families ($p \leq 0.05$) are highlighted.
**C.** Boxplot showing loop strength across five TF families. The LSD multiple comparison test was used to assess significance. Different letters denote significant differences ($p \leq 0.05$).
**D.** Percentage of TF binding sites enriched in functional hub anchor regions. Calculated as: TF binding site identified in functional hubs/TF binding sites identified in all hubs.
**E.** Boxplot showing the average number of target genes (TF binding motifs in promoter regions) per hub anchor or functional hub anchor across five TF families. *, $p \leq 0.05$; **, $p \leq 0.01$ from Student's *t*-test.
**F.** Expression levels of genes categorized by chromatin interaction models and SBP occupancy. The LSD multiple comparison test was used to assess significance. Different letters indicate significant differences ($p \leq 0.05$).

**TaSPL7/15-mediated chromatin interactions regulate photosynthesis and leaf development in wheat**

Given the critical role of *TaSPL7* and *TaSPL15* in wheat's vegetative and reproductive

453 growth, mutant lines with a higher number of SPB mutations provide a clearer
454 understanding of the loops mediated by SBP TF, we analyzed the CRISPR/Cas9-
455 derived knockout mutant *Taspl7&15* (*61*) and conducted RNA-seq on *Taspl7&15* and
456 wild-type (WT) counterpart, ZM7698. Transcriptomic analysis revealed strong
457 correlations among replicates (**Fig. 6A**) and identified 1,917 down-regulated and 1,802
458 up-regulated genes in *Taspl7&15*. GO enrichment indicated pathways related to
459 chloroplasts, leaf development, and carbohydrate transport were significantly affected,
460 underscoring TaSPL7/15's role in photosynthesis and leaf development (**Fig. 6B**).

461 To reveal the role of TaSPL7/15-mediated loops on transcriptional regulation, we
462 defined loops in which both the left and right anchors overlap with TaSPL7/15 DAP-
463 seq peaks as TaSPL7/15-mediated loops. Active histone marks such as H3K4me3,
464 H3K9ac, and H3K27ac, as well as the inhibitory mark H3K27me3, were enriched in
465 TaSPL7/15-mediated loop anchors (**fig S6**). This suggests that the TaSPL7/15-mediated
466 loop may be regulated through the interaction of multiple histone modification signals,
467 possibly reflecting a complex and coordinated regulatory mechanism. Approximately
468 48% of differentially expressed genes (DEGs) overlapped with TaSPL7/15-mediated
469 chromatin loop-associated genes, suggesting that TaSPL7/15 maintains chromatin
470 loops critical for gene expression (**Fig. 6C and table S4**). These loop-associated DEGs
471 were significantly enriched in functional regulatory QTLs, highlighting their
472 importance (**Fig. 6D**). Key loop-associated DEGs included chlorophyll a-b binding
473 protein 5 (*TaLhcb5-6D*) (up-regulated), chlorophyll degradation gene *Stay-Green Rice*
474 (*TaSGR-5D*) (down-regulated), and stomatal anion channel protein controlling stomatal
475 closure gene *SLOW ANION CHANNEL-ASSOCIATED 1* (*TaSLAC1-D1*) (down-
476 regulated), all influencing chlorophyll content and photosynthetic efficiency (**Fig. 6E,**
477 **table S5**). Additionally, transketolase (TaTK-2D), positive regulator of starch
478 accumulation in vegetative tissues $CO_2$-responsive CCT protein (TaNRR-A1), were up-
479 regulated, while negative regulators of leaf development, such as cytokinin
480 oxidase/dehydrogenase 11 (TaCKX11-A) and (*TaCKX11-B*), were down-regulated.

481 To validate these chromatin interactions, we focused on *TaCKX11-B*, a gene previously
482 linked to negative regulation of leaf size and photosynthetic efficiency in rice and wheat
483 (*62*), (*56*). A 57-kb upstream interaction loop was identified in WT (ZM7698) but lost
484 in *Taspl7&15* (**Fig. 6F**). 3C-qPCR confirmed the loss of this interaction loop in
485 *Taspl7&15* (**Fig. 6G, upper**), and RT-qPCR demonstrated reduced *TaCKX11-B*
486 expression (**Fig. 6G, lower**). Luciferase reporter assays validated the enhancer-like
487 function of the distal region on *TaCKX11-B* (**Fig. 6H**). Similar loop disruption were
488 observed for *TaSGR-5D*, *TaNRR-A1,* and *TaTK-2D* (**fig. S7A-C**).

489 Phenotypic analysis showed *Taspl7&15* mutants had larger leaf size, higher chlorophyll
490 content, and improved photosynthetic efficiency (**Fig. 6I, J**). Liquid chromatography-
491 mass spectrometry (LC-QQQ-MS) analysis revealed increased levels of photosynthetic
492 intermediates, including pentose phosphate (D-Ribose 5-phosphate (R5P), ribulose-5-
493 phosphate (Ru5P), D-Xylulose-5-phosphate (Xu5P), and D-Sedoheptulose-7-
494 phosphate (S7P) in *Taspl7&15* compared to ZM7698 (**fig. S8**), indicating enhanced
495 photosynthetic capacity. Notably, the absence of phosphoglycerate 3-phosphoglycerate
496 (3PGA) and 2-phosphoglycerate (2PGA) suggested reduced photorespiratory flux,
497 potentially boosting photosynthetic efficiency (**fig. S8**). Moreover, we observed larger
498 starch granules in *Taspl7&15*' leaves than in those of ZM9867 (**Fig. 6K**). Those
499 phenotypic data fit well with the observed transcriptional change of above-mentioned
500 genes in *Taspl7&15*.

In summary, TaSPL7/15 mediates chromatin interactions critical for regulating photosynthesis-related genes and leaf development. Loss of TaSPL7/15 disrupts these loops, altering gene expression and enhancing photosynthetic efficiency in wheat leaves.

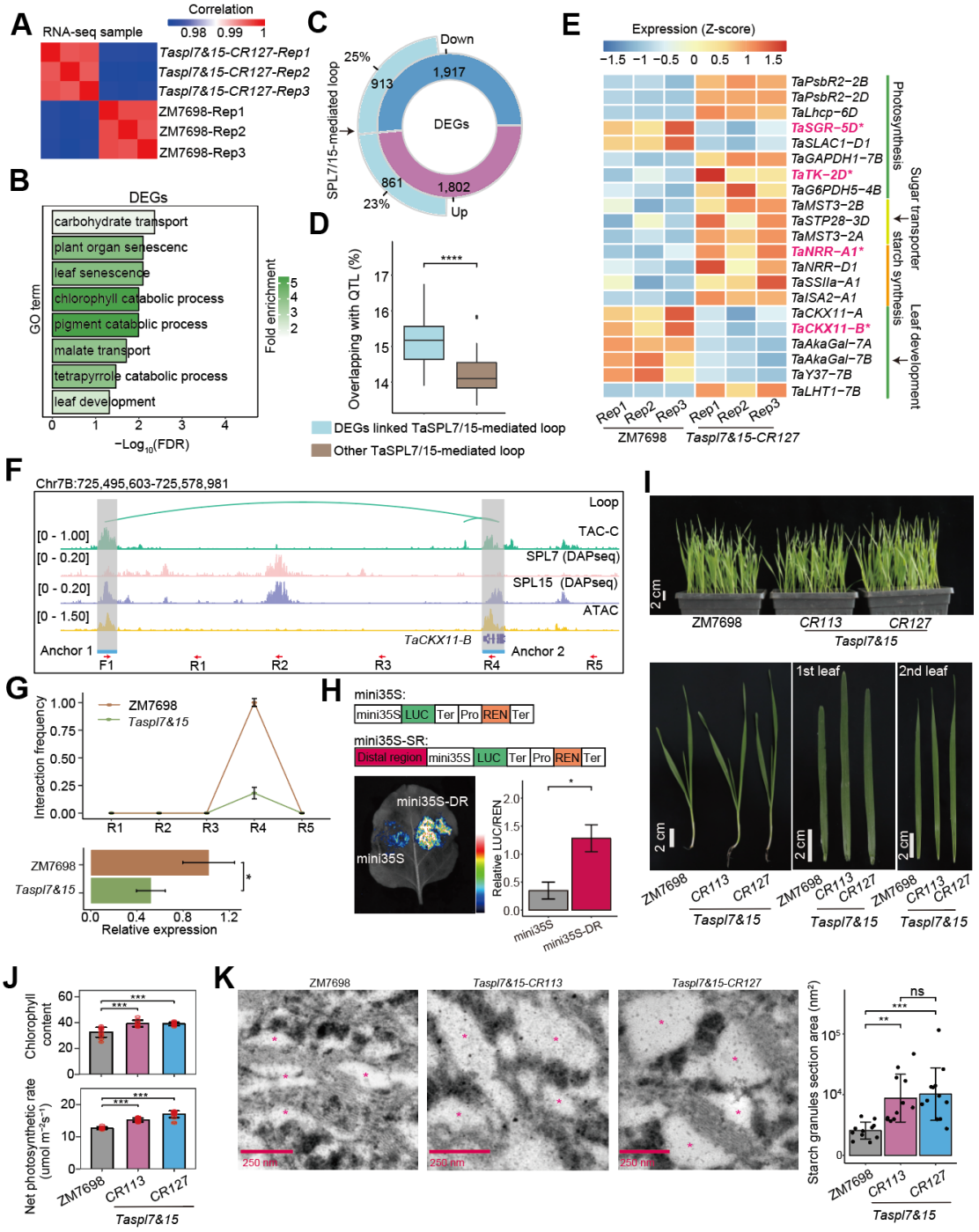


**Fig. 6 SPL-associated chromatin interactions in regulating photosynthetic energy metabolism**

**A.** Clustering of samples for RNA-seq according to the person correlation coefficient of gene expression levels.

**B**. GO enrichment analysis of DEGs in *Taspl7&15* vs ZM7698.

**C.** Proportion of DEGs overlapped with TaSPL7/15-mediated chromatin loop linked genes.

513 **D.** The percentage of overlapped interactions between TaSPL7/15-mediated loop linked
514 DEGs and other TaSPL7/15-mediated loop. ***, $p \leq 0.001$ from Student's *t*-test.
515 **E.** Heatmap displaying the expression of key genes involved in photosynthesis and leaf
516 development. Expression levels were normalized by *z*-score. The genes that are further
517 validated in the following are highlighted.
518 **F.** Browser screenshot showing chromatin loop interactions of *TaCKX11-B.* Profiles of
519 TaSPL7/15 DAP-seq, ATAC, and chromatin interactions around *TaCKX11-B* and its
520 distal regulatory site are shown, with anchor regions highlighted. The lower panel
521 shows the locations of primer in 3C-qPCR experiments.
522 **G.** The upper panel is the quantitative relative interacting frequency of loop regions
523 determined by 3C-qPCR in ZM7698 and *Taspl7&15*. The lower panel is the
524 quantitative relative expression of *TaCKX11-B* by RT-qPCR assay in ZM7698 and
525 *Taspl7&15*. Error bars: ±SD, *, $p \leq 0.05$ from Student's *t*-test.
526 **H.** Luciferase reporter assay validating the transcriptional regulatory role of the distal
527 regions (DR) on *TaCKX11-B*. The distal anchor sequence was introduced into the
528 proximal region of the *TaCKX11-B* promoter. *, $p \leq 0.05$ from Student's *t*-test.
529 **I.** Phenotypes of leaves of the wheat accession ZM7698 and two CRISPR-generated
530 *Taspl7&15* mutant lines (*CR113* and *CR127*) at the seedling stage.
531 **J.** Comparison of chlorophyll content, and net assimilation rates of carbon dioxide
532 between ZM7698 and the two CRISPR lines of *Taspl7&15* mutant at the seedling stage.
533 ***, $p \leq 0.001$ from Student's *t*-test.
534 **K.** Transmission electron microscopy (TEM) images of chloroplasts of for ZM7698
535 and *Taspl7&15* two mutant lines. Red asterisks indicate starch granules. The area of the
536 starch granules section is calculated by ImageJ. **, $p \leq 0.01$; ***, $p \leq 0.001$ from
537 Student's *t*-test.

538 **Discussion**

539 Understanding the spatial organization of *cis*-regulatory elements (CREs) is essential
540 for deciphering gene regulation (*63*), particularly in complex genomes like wheat, a
541 hexaploid species (*29*). The three-dimensional structure of the genome plays a crucial
542 role in how CREs, such as enhancers, interact with their target genes to control key
543 biological processes (*44, 64*). Traditional methods like Hi-C, HiChIP, and OCEAN-C
544 have advanced our understanding of chromatin interactions but have been less effective
545 in capturing the fine-scale interactions between CREs and genes in wheat (*25, 28, 30*).

546 **TAC-C: A plant specialized fine-scale 3D chromatin organization study tool**

547 Due to the higher spatial resolution of ATAC-seq compared to FAIRE-seq (*27*), we
548 developed the TAC-C method by integrating ATAC-seq with *in situ* Hi-C, facilitating
549 targeted capture of interactions within open chromatin regions. This advancement not
550 only heightens spatial resolution but also reduces the sequencing depth required to yield
551 meaningful data. This innovation holds particular significance for cost reduction,
552 especially in the context of crops with large genomes like wheat. TAC-C excels in
553 identifying active *cis*-regulatory elements and demonstrates better overlap with
554 epigenetic modifications compared to other methods (**Fig. 1**). Using wheat as a model,
555 TAC-C has proven its robustness in capturing intricate details of chromatin interactions
556 that are crucial for understanding gene regulation in large-genome species. The
557 method's adaptation for plant samples, particularly those rich in sugars and
558 polyphenols, further underscores its versatility and reliability. Unlike the recently
559 developed ChIATAC technique (*18*), TAC-C omits the use of SDS in nuclei treatment
560 (**Fig. 1**). SDS as a surfactant, has the potential to disrupt the binding between histones

561 and DNA. This disruption facilitates Tn5 accessibility to closed chromatin regions.
562 Consequently, compared to the ChIATAC, TAC-C is more similar to ATAC-seq.
563 Moreover, ChIATAC was only used in animal cells, with no reported application in
564 plants, while TAC-C is a technology tailored specifically for plant systems. These
565 makes TAC-C not only a powerful alternative but also a more specialized tool for
566 studying the 3D genome organization in plants. The success of TAC-C in rice, wheat,
567 maize, sorghum (**Fig. 2**) suggests its potential applicability across other complex
568 genomes, providing a new avenue to explore the spatial organization and regulatory
569 mechanisms underlying large-genome species.

570 **Conservation and biological importance of TAC-C identified chromatin**
571 **interaction hub anchors**

572 TAC-C identifies open chromatin regions frequently interacting with other regions,
573 termed hub anchors (**Fig. 2**). Across different crops species, hub anchors exhibit
574 common features such as low-frequency base variations and higher expression levels
575 of their associated node genes (**Fig. 2**). Moreover, a significant overlap was observed
576 between previously reported QTL, eQTL, and breeding selection intervals with
577 chromatin interaction anchors, especially hub anchors (**Fig. 3**). This underscores the
578 functional importance of open chromatin interactions in regulating agronomic traits.
579 GWAS has identified numerous QTLs in crops with large genomes like maize and
580 wheat (*65, 66*), often located in intergenic regions, complicating their functional
581 interpretation. Chromatin interactions can be used as physical evidence to connect
582 GWAS-identified SNPs to their target genes, offering insights into trait-associated
583 elements. For example, our study revealed chromatin interactions between *TaNAL1-*
584 *5A-like* and its eQTL loci (**Fig. 3**). This research advances our understanding and paves
585 the way for precision breeding using advanced editing technique.

586 **Chromatin spatial organization contributes to subgenome gene expression bias**

587 Previous research has demonstrated that differences in epigenetic modifications,
588 transposon insertions, and TF binding motifs significantly influence homoeolog
589 expression bias in wheat (*41, 58, 72, 73*). Our TAC-C data support these findings,
590 revealing extensive subgenome-specific PPIs (**Fig. 4**). Notably, the D subgenome
591 exhibited more chromatin interactions compared to the A and B subgenomes (**Fig. 4**),
592 possibly due to the latter undergoing epigenetic homogenization over time (*74*). In
593 contrast, the D subgenome, with its shorter evolutionary history, may retain more
594 diploid-like epigenetic features.

595 Our results also show an enrichment of transposons in subgenome-specific interaction
596 anchors (**Fig. 4**), suggesting that some transposons have evolved into regulatory
597 elements, influencing subgenome-specific gene expression through chromatin looping
598 (*60, 73, 75*). While previous studies focused on genetic sequence variations and
599 epigenetic modifications (*41, 60, 76*), our research highlights the importance of distal
600 chromatin interactions in shaping subgenome bias (**Fig. 4**). Previous studies showing
601 that gene expression bias was not observed in homoeologous genes with chromatin
602 interaction divergence (*28*). However, in our study, we clearly observed that
603 homoeologous genes in subgenomes with chromatin loop loss exhibit significantly
604 lower expression levels compared to other subgenomes. This discrepancy may be due
605 to the higher precision and resolution of TAC-C, which enables the detection of subtle
606 imbalances in chromatin loops between subgenomes. We propose that sequence
607 variations and transposon insertions near homoeologous genes modify the chromatin
608 environment, leading to biased gene expression and reinforcing subgenome

609 imbalances. This asymmetric chromatin interaction offers new insights into the
610 regulation of subgenome bias in hexaploid wheat and presents opportunities for
611 developing precise gene regulation strategies at the subgenome level.

612 **SBPs in chromatin organization and wheat development**

613 While CTCF/cohesin complexes control chromatin loops in animals (*35, 36*), and TCPs
614 shape chromatin structure in *Marchantia* (*40*), the processes governing chromatin loops
615 in higher plants like wheat are not well understood (*77*). TaSPL7/15 participate in wheat
616 vernalization process by directly anchoring the *VERNALIZATION1* (*VRN1*) promoter
617 and 30Kb upstream regulatory elements of *VRN3* (*78*), yet their broader role in wheat
618 3D chromatin structure has been unexplored. Our findings reveal an enrichment of SBP
619 and ERF TF binding motifs in chromatin's open anchor regions (**Fig. 5**), indicating the
620 potential role in maintaining wheat chromatin organization. In *Taspl7&15* mutants, a
621 substantial overlap was observed between differentially expressed genes and
622 TaSPL7/15-mediated loop linked genes (**Fig. 6**), particularly those involved in
623 photosynthesis, starch synthesis, sugar transport, and leaf development (**Fig. 6**), leading
624 to increased photosynthetic efficiency in *Taspl7&15*. Specifically, the loss of distal
625 regulatory interaction for *TaCKX11-A*, *TaCKX11-A*, *TaSGR-5D*, *TaTK-2D* and *TaISA2*
626 resulted in longer leaves, reduced chlorophyll degradation, enhancing photosynthesis
627 efficiency and increased photosynthetic products (**Fig. 6**). Additionally, SPLs are
628 quantitatively regulated by miRNA156s, conserved microRNAs associated with plant
629 developmental ages across species (*79, 80*), suggesting that 3D chromatin organization
630 may undergo SPL-mediated change as plants mature, contributing to developmental
631 morphology.

632 **Methods**

633 **Plant materials and growth conditions**

634 The *O. sativa*, *S. bicolor*, *Z. mays* and *T. aestivum* (Chinese Spring) were used in this
635 study. For the *Taspl7&15* CRISPR lines which we got from previous study (*61*). The
636 seeds were surface sterilized in 2% NaClO for 20 minutes, then rinsed overnight with
637 flowing water. The seeds were germinated and then transferred to soil, and grown in
638 the greenhouse at 22°C/20°C day/night, under long day conditions (16h light/8h dark).
639 When the material grows to one leaf and one heart period, the leaves were sampled for
640 the RNA-seq (three replicates), and TAC-C experiments (two replicates).

641 **TAC-C library construction**

642 TAC-C experiments require three processions, including:

643 Plant tissue was cut into approximately 0.5 square centimeter pieces, and then fixed
644 using Nuclei Isolation Buffer (NIB) containing 4% formaldehyde (20mM Hepes,
645 250mM Sucrose, 1mM $MgCl_2$, 5mM KCl, 1mM DTT, 1% Protease Inhibitor Cocktail
646 for Plants, 0.25% Triton X-100, 40% glycerol, 4% formaldehyde). The reaction was
647 quenched by adding 0.125 M glycine and incubated on ice for 15 minutes. The fixed
648 plant tissue was washed three times with NIB (20mM Hepes, 250mM Sucrose, 1mM
649 $MgCl_2$, 5mM KCl, 1mM DTT, 1% Protease Inhibitor Cocktail for Plants, 0.25% Triton
650 X-100, 40% glycerol). After removing excess liquid from the surface using absorbent
651 paper, nuclear extraction could be performed directly, or the samples could be stored at
652 -80℃.

653 The processed plant tissue, subjected to liquid nitrogen grinding, was transferred to a
654 15mL tube, and the pellets were then resuspended using NIB. The suspension was

incubated with shaking on ice for 10 minutes. Subsequently, the suspension was successively filtered through 10μm and 40μm strainers, followed by centrifugation at 1260g at 4℃ for 5 minutes. After discarding the supernatant, the pellets were washed twice with NIB and then washed twice with 1.2×NEBuffer r2.1 (NEB; B6002S). Nuclei were obtained after centrifugation at 1260g at 4℃ for 5 minutes with the removal of the supernatant. The isolated nuclei can be used for TAC-C library preparation or stored at -80℃.

Using 10,000 to 50,000 nuclei as the starting material for TAC-C library construction. The nuclei were resuspended in 500μL 1.2× NEBuffer r2.1, and 40μL DpnII (NEB; R0543L) was added. The reaction was carried out overnight at 37℃ with constant agitation at 900rpm in a metal bath. Subsequently, the reaction was terminated by incubating at 65℃ for 20 minutes. After that, 37.5μL Biotin-14-dCTP (Invitrogen; 19518018), 1.5μL 10mM dATP (NEB; N0446S), 1.5μL 10mM dTTP (NEB; N0446S), 1.5μL 10mM dGTP (NEB; N0446S), and 10μL DNA Polymerase I, Large (Klenow) Fragment (NEB; M0210L) were added, and the reaction was carried out at 37℃ for 1h in a metal bath to complete biotin labeling. Following this, 598μL 2× Rapid Ligation Buffer and 6 μL T4 DNA ligase (Enzymatics; L6030-HC-L) were added, and the reaction was carried out at 20℃ for 4h to complete the *in situ* ligation. The reaction mixture was centrifuged at 5000g for 5 minutes, the supernatant was discarded, and the nuclear pellet was resuspended in TE Buffer (pH 10, invitrogen, AM9858), incubated at 70℃ for 1 hour. The reaction mixture was centrifuged at 1000g for 5 minutes, and 1μL Exonuclease III (NEB; M0206), 10μL 10×NEBuffer1 (NEB; M0206), and 89μL Nuclease-Free Water were added. The reaction was carried out at 37℃ for 20 minutes, followed by 72℃ for 30 minutes to terminate the reaction. After washing once with 500μL 1×TD buffer (10mM Tris-HCl, pH 7.4, 5mM $MgCl_2$, and 0.25% Dimethyl Formamide), the samples were centrifuged at 1260g for 5 minutes, and the supernatant was discarded. Then, 50μL 2×TD Buffer (20mM Tris-HCl, pH 7.4, 10mM $MgCl_2$, 0.5% Dimethyl Formamide) and 8μL TTE Mix V50 (Vazyme; TD711-02), 42μL Nuclease-Free Water were added, and the reaction was carried out at 900rpm, 37℃ for 1h in a metal bath. After the reaction, the DNA was purified using the MinElute PCR Purification Kit (Qiagen; 28004), washed with 100μL Buffer EB (Qiagen; 19086), and then incubated with 40μL Dynabeads MyOne Streptavidin C1 (Invitrogen; 65001) at room temperature for 20 minutes. The beads were washed twice with Binding and Washing Buffer (5mM Tris-HCl, pH 7.5, 0.5mM EDTA, 1M NaCl). Finally, the DNA was amplified by adding 50μL TruePrep CUT&Tag Amplification Mix (Vazyme; TD612-01), 40μL Nuclease-Free Water, 5μL 20uM N7 index primer (TGTGAGCCAAGGAGTTGTTGTCTTCNNNNNNNNNNGTCTCGTGGGCTCGG), and 5μL 20uM N5 primer (/5Phos/GAACGACATGGCTACGATCCGACTTTCGTCGGCAGCGTC). The amplification conditions were as follows: 72℃ for 5 minutes, 98℃ for 30 seconds; 98℃ for 10 seconds, 63℃ for 30 seconds, 72℃ for 1 minute, 10 cycles; 72℃ for 5 minutes; hold at 4℃. The PCR products were purified using 60μL Ampure beads (Beckman Coulter; A63881), incubated for 5 minutes, placed on a magnetic stand for 5 minutes, and then the supernatant was transferred to a new 1.5mL tube. After incubating with 20μL Ampure beads for 5 minutes and placing on a magnetic stand for 5 minutes, the supernatant was discarded. The beads were washed twice with 80% ethanol, and after the beads were air-dried, the DNA was recovered using Buffer EB. This is the TAC-C library. The TAC-C library was sequenced using MGI 2000

703 (2×100bp). The relevant chemicals and enzymes are listed in **table S6**.

704 **RNA-seq library construction**

705 Total RNAs were extracted using Ultrapure RNA kit (CWBIO; CW0581M) according
706 to manufacturer instructions. The products were sequenced using an Illumina
707 NovaSeq6000 by Gene Denovo Biotechnology and RNA-seq data were obtained from
708 three biological replicates.

709 **TAC-C data processing**

710 Initially, the raw reads underwent trimming using the hicup_truncater v0.5.9 tool (*81*)
711 to identify and eliminate the ligated junction points within the reads, specifically
712 removing the sequences after the recognition site of restriction enzyme. Subsequently,
713 the trimmed reads were mapped to the reference genome: *S. bicolor* (*82*), *Z. mays* (*83*),
714 *O. sativa* (*84*) and *T. aestivum* (*85*) through the bwa v0.7.17 software (*86*), with reads
715 having a mapping quality (MAPQ) score<1 being discarded to ensure mapping
716 accuracy. The Hi-C-Pro v2.10.0 (*87*) tool was employed to filter out Dangling End
717 Pairs, Re-ligation Pairs, Self-cycle Pairs, and Dumped Pairs. Following the removal of
718 PCR duplicates, the remaining valid read pairs were used for calling peaks and loops.
719 The calling of peaks from the remaining valid read pairs was performed using MACS2
720 (*88*) the parameter "-q 0.01 -f BAM --nomodel --extsize 150 --shift -75 --call-summits
721 --nolambda", The overlapping peaks between two biological replicates were used as an
722 anchor to identify open chromatin interactions by hichipper
723 (http://aryeelab.org/hichipper) with default setting in two biological replicates. Finally,
724 the intrachromosomal loop from two biological replicates were merged by
725 hicMergeLoops from HiCExplorer software (*89*) with the parameter "-r 10000". TAC-
726 C interaction heatmaps were produced with HiCPlotter v0.8.1 at 1-Mb resolution (*90*).

727 **OCEAN-C and Hi-C data processing**

728 We downloaded the OCEAN-C and Hi-C data of Chinese Spring from the NGDC
729 BioProject database (accession number CRA003731) and NCBI (accession number
730 GSE133885) (*25, 28*). Reads were aligned to the IWGSC RefSeq v2.1 reference
731 genome. The data analysis procedures are the same with the analysis for TAC-C data.
732 In particular, for the Hi-C intrachromosomal loops, we directly use the published results
733 of previous study (*30*).

734 **RNA-seq data analysis**

735 Low-quality reads and adapter sequences were removed using Cutadapt (*91*) and
736 Trimmomatic (*92*), respectively. Retained clean RNA-seq reads were mapped to the
737 same version reference genome with TAC-C by using STAR(*93*) (version 2.5.4b) with
738 default parameters: SortedByCoordinate --quantMode TranscriptomeSAM
739 GeneCounts, and accurate transcript was quantified using RSEM (*94*) (version 1.3.0).
740 In addition, RSEM was also used to analyze the mRNA expression level by calculating
741 Fragments per Kilobase of exon model per Million (FPKM) mapped reads. The RNA-
742 seq reads counts of DEGs were filtered with $|\log_2(\text{fold change})|>0$ and FDR<0.05 by
743 using R packages edgeR (*95*).

744 **Gene ontology analysis**

745 The GO functional enrichment was performed using the find_enrichment.py from
746 goatools software (*96*).

747 **ChIP-seq and ATAC-seq data analysis**

748 Sequencing reads of H3K4me3, H3K9ac, H3K27ac, H3K27me3, H3K9me3,
749 H3K36me3 and ATAC-seq of Chinese Spring were obtained from previous studies (*28,*
750 *41*). ChIP-seq data are available in NCBI GEO under accession number GSE121903
751 and ATAC-seq data are available in NGDC GSA under accession number CRA003731.
752 Sequencing reads were cleaned by removing bases that had low quality scores (<20)
753 and removing sequencing adaptors by Cutadapt (*91*) and filtering out short reads by
754 Trimmomatic (*92*). The reads of ChIP-seq and ATAC-seq were mapped to the IWGSC
755 RefSeq v2.1 reference genome using Bowtie2 (*97*) with default setting. The
756 concordantly mapped reads (MAPQ>10) were kept and PCR duplication was further
757 removed with Picard (https://broadinstitute.github.io/picard/). Peaks of ChIP-seq
758 libraries were detected using MACS2 (2.1.2) with the parameter "-f BAM –nomodel -
759 q 0.05". The peaks of ATAC-seq were identified using MACS2 with the parameter "-q
760 0.05 -f BAM --nomodel --extsize 200 --shift -100".

761 **DAP-seq data analysis**

762 For SPL7A, SPL7B, SPL7D, SPL15A, SPL15B and SPL15D DAP-seq data analysis,
763 the raw sequencing reads (from the NCBI accession number PRJNA779959) (*61*) were
764 cleaned by removing bases that had low quality scores (<20) and removing sequencing
765 adaptors by Cutadapt (*91*), and filtering out short reads by Trimmomatic (*92*). As a
766 result, about 5 million reads with a MAPQ score>20 was obtained for further analyses.
767 The cleaned reads were mapped to the IWGSC RefSeq v2.1 reference genome using
768 Bowtie2 (*97*) (version 2.4.4) with default settings. MACS2 (*88*) was used for peak
769 calling of the ChIP-Seq datasets, with options: -g 7.83e8 --call-summits --bdg -q 0.01 -
770 -nomodel. Typical DAP-seq loci were plotted using Integrative Genomics Viewer
771 solftware (*98*).

772 For ERF, Dof, MYB and other SPL DAP-seq peak were download from GSE192815
773 and GSE188699 (*60, 61, 73*). The overlap of DAP-seq peak with anchor were
774 calculated using BEDTools (*99*) with parameter: intersect -wa -wb.

775 **Identification of homoeolog PPIs**

776 The interspecies syntenic genes and homologous genes were download from TGT
777 (http://wheat.cau.edu.cn/TGT/) across four species (*100*). PPIs whose anchors on one
778 side were homologous genes between two species and anchors on another side was also
779 homologous genes were defined as homologous PPIs, and the corresponding genes are
780 defined as homologous PPI genes. The PPI homologous in *S. bicolor* and *Z. mays* (*83*)
781 were defined as C4 conserved PPIs; PPI homologous in *O. sativa* and *T. aestivum* were
782 defined as C3 conserved PPIs.

783 High-confidence gene models from the IWGSC (version 1.0) were used for defining
784 triad genes. Homoeolog genes between each pair of A, B, and D subgenomes were
785 identified as previously described (*58*). The Gene ID from IWGSC (version 1.0) were
786 converted to IWGSC (version 2.1) by TGT (http://wheat.cau.edu.cn/TGT/) (*100*). Then
787 a total 18,333 homoeolog groups with only one gene copy in each subgenome were
788 defined as triads. PPIs whose anchors on one side were homoeolog genes between A,
789 B, or D subgenomes and anchors on another side was also homoeolog genes were
790 defined as homoeolog PPIs, and the corresponding genes are defined as homoeolog PPI
791 genes.

792 **TF Motif analysis**

793 We use Homer (*101*) to find enrichment of sequence motifs with default parameters.
794 Sequences in TAC-C anchor in were used as input. The "Known Results" were used as
795 final results. The enriched TF motifs were further used for TF family enrichment
796 analysis. Enrichment analysis was done using the R package clusterProlifer (v3.16.1)
797 (*102*), with a threshold $P_{adj} < 0.05$. The set of 1,007 "known TF motifs" from Homer
798 and their families served as the background, and enrichment was calculated by enricher
799 function.

800 **RT-qPCR and 3C-qPCR**

801 Total RNA was extracted using HiPure Plant RNA Mini Kit according to the
802 manufacturer's instructions (Magen; R4111-02). First-strand cDNA was synthesized
803 from 2μg of DNase I-treated total RNA using the TransScript First Strand cDNA
804 Synthesis SuperMix Kit (TransGen; AT301-02). RT-qPCR was performed using the
805 ChamQ Universal SYBR qPCR Master Mix (Vazyme; Q711-02) by QuantStudio5
806 (Applied biosystems). The expression of interested genes was normalized to Tubulin
807 for calibration, and the relative expression level is calculated via the $2^{-\Delta\Delta CT}$ analysis
808 method (*103*). Primers used for RT-qPCR are listed in **table S7**.

809 To calculate the relative interaction frequencies between two regions, 3C-qPCR
810 validation was performed following previously described methods (*104*). A genomic
811 region without DpnII digestion was amplified as a loading control to normalize the
812 DNA concentrations of different samples. Primers used for 3C-qPCR are listed in **table**
813 **S7**.

814 **Luciferase reporter assay**

815 To generate the p*TaNAL1-like-5A*:LUC construct, we amplified 3-Kb promoter
816 fragments upstream of *TaNAL1-like-5A* from CS and ligated them with the transient
817 expression vector CP461-LUC, which was constructed as the reporter vector. The
818 p35S-*Traes5A02G000700*-GFP construct was used as effector. Then, p*TaNAL1-like-*
819 *5A*:LUC and p35S:*Traes5A02G000700*-GFP were transformed into *A. tumefaciens*
820 strain GV3101. The p*TaNAL1-like-5A*:LUC and p35S-pro:GFP were co-transformed as
821 controls.

822 To generate *PR*-mini35Spro:LUC construct, the genomic sequence of distal regulatory
823 region was amplified and fused in-frame with the pMY155-mini35S vector to generate
824 the reporter construct. Then, mini35Spro:LUC (as control) and *PR*-mini35Spro:LUC
825 were transformed into *A. tumefaciens* strain GV3101.

826 Then these strains were injected into *N. benthamiana* leaves (6~8 leaf stage) in different
827 combinations with p19, which was used to suppress RNA silencing. Dual luciferase
828 assay reagents (Promega; VPE1910) with the Renilla luciferase gene as an internal
829 control were used for luciferase imaging. The Dual-Luciferase Reporter Assay System
830 kit (Promega; E2940) was used to quantify fluorescence signals. Relative LUC activity
831 was calculated by the ratio of LUC/REN. The relevant primers are listed in **table S7**.

832 **Measurement of photosynthetic capacity, chlorophyll content, and leaf area**

833 The measurement of photosynthetic capacity was conducted on the *Taspl7&15-CR*
834 lines. The penultimate new leaves fully expanded were selected for the measurement
835 of net photosynthesis rate with a portable gas-exchange and fluorescence system (GFS-
836 3000, Walz, Germany). The environmental parameters were set as follows: an air-flow
837 of 400 mmol $s^{-1}$ through the chamber, a leaf temperature of 25°C, a $CO_2$ concentration

838 of 400 μmol $mol^{-1}$.

839 Chlorophyll content was measured with the same penultimate new fully expanded
840 leaves at room temperature with a TYS-B Chlorophyll meter (Zhejiang TP, China).

841 Leaf area was measured with the same penultimate new fully expanded leaves at room
842 temperature with a Yaxin-1241 portable Leaf Area Meter (Beijing Yaxinliyi Science
843 and Technology Co. Ltd., China).

844 **Liquid Chromatography-Mass Spectrometry analysis**

845 The endogenous levels of R5P/Ru5P/Xu5P, 3PGA/2PGA, E4P, DHPA, S7P, F6P/G1P
846 and G6P were determined with an ultra-performance liquid chromatography-tandem
847 mass spectrometry analytical platform consisting of an Agilent 1290 Infinity liquid
848 chromatography pump and a 6495 triple quadrupole mass spectrometer (Agilent
849 Technology Co. Ltd., America), following the protocol described in previous study
850 (*105*).

851 **Ultrathin sections and scanning electron microscopy**

852 Ultrathin (70nm) sections of ZM9867 and *Taspl7&15-CR* leaves were prepared using
853 a Leica EM UC7 ultramicrotome (Leica, Vienna, Austria), as previously described
854 (*106*). Sections were placed on formvar-coated copper grids and poststained with uranyl
855 acetate and lead citrate and observed under a HT-7700 transmission electron
856 microscope (Hitachi, Tokyo, Japan) operated at 80 kV.

857 **Statistics and data visualization**

858 If not specified, R (https://cran.r-project.org/; version 4.3.2) was used to compute
859 statistics and generate plots. For the two groups' comparison of data, the Student's *t*-
860 test was used such as Fig. 2, 3, 4, 5, 6, 7 and fig. S2, 3 and 4. For three or more
861 independent groups comparison of data, Fisher's Least Significant Difference was used,
862 such as Fig. 3B, 5C and 5F. Pearson correlation was used in Fig. S1A. For enrichment
863 analysis, Fisher's exact test was used, such as Fig. 5B, 6B, fig. S2H, fig. S3C and S3D.
864 The Integrative Genomics Viewer (IGV) was used for the visual exploration of genomic
865 data, such as Fig. 1I, 2I, 3F, 4I, 6F and fig. S5A-C

866 **Data and materials availability**

867 Sequencing data of TAC-C, and RNA-seq are available at Genome Sequence Archive
868 of the National Genomics Data Center, China National Center (PRJCA029954) and are
869 publicly accessible at https://ngdc.cncb.ac.cn/gsa. Code used for all processing and
870 analysis is available in GitHub (https://github.com/ZhangZhaoheng24/TAC-C).

871 **Acknowledgements**

872 We thank Prof. Yiping. Tong (Institute of Genetics and Developmental Biology,
873 Chinese Academy of Sciences) for the *Taspl7&15*-CR mutants and Dr. Chunyan Zhang
874 (Plant Science Facility of the Institute of Botany, Chinese Academy of Sciences) for the
875 help on the measurement of photosynthetic capacity, Prof. Yue Zhou (Peking
876 University) for the comments on the manuscript.

877 **Funding**

878 This research was supported by the National Science and Technology Major Project
879 (2023ZD04073), the National Key Research and Development Program of China
880 (2021YFD1201500), the Beijing Natural Science Foundation Outstanding Youth
881 Project (JQ23026) and the CAS Project for Young Scientists in Basic Research (YSBR-

093).

## Author contributions

J.X. designed and supervised the research. J.X., Z.-H.Z., X.-L.L. and J.-M.K. wrote the manuscript. J.-M.K. developed and tested the TAC-C technology. X.-L.L. did the sample collection, mutants phenotype and physiological experiments. J.-M.K. and Y.-L.S. did TAC-C experiments. X.-M.L. did transcription regulation assay. Z.-H.Z., F.-Y.L., P.Z. and Y.-J.L. performed data analysis. X.-Y.L., Y.-Y.L. and W.-D.W. helped for the photosynthetic phenotypic analysis. C.-M.L., S.-B.X. and X.L. revised the manuscript. Z.-H.Z., X.-L.L. and J.X. prepared all the figures. All authors discussed the results and commented on the manuscript.

## Competing interests

The authors declare no competing interests.

## References


1. A. Hendelman *et al.*, Conserved pleiotropy of an ancient plant homeobox gene uncovered by cis-regulatory dissection. *Cell* **184**, 1724-1739.e1716 (2021).
2. R. J. Schmitz, E. Grotewold, M. Stam, Cis-regulatory sequences in plants: Their importance, discovery, and future challenges. *The Plant Cell* **34**, 718-741 (2021).
3. A. P. Marand, A. L. Eveland, K. Kaufmann, N. M. Springer, cis-Regulatory Elements in Plant Development, Adaptation, and Evolution. *Annu. Rev. Plant Biol.* **74**, 111-137 (2023).
4. X. Lin *et al.*, Systematic identification of wheat spike developmental regulators by integrated multi-omics, transcriptional network, GWAS, and genetic analyses. *Mol Plant* **17**, 438-459 (2024).
5. X. Bai *et al.*, Duplication of an upstream silencer of FZP increases grain yield in rice. *Nat Plants* **3**, 885-893 (2017).
6. R. M. Clark, T. N. Wagler, P. Quijada, J. Doebley, A distant upstream enhancer at the maize domestication gene tb1 has pleiotropic effects on plant and inflorescent architecture. *Nat. Genet.* **38**, 594-597 (2006).
7. J. O. Melo *et al.*, Repeat variants for the SbMATE transporter protect sorghum roots from aluminum toxicity by transcriptional interplay in cis and trans. *Proc Natl Acad Sci U S A* **116**, 313-318 (2019).
8. S. L. Klemm, Z. Shipony, W. J. Greenleaf, Chromatin accessibility and the regulatory epigenome. *Nat Rev Genet* **20**, 207-220 (2019).
9. G. E. Crawford *et al.*, Genome-wide mapping of DNase hypersensitive sites using massively parallel signature sequencing (MPSS). *Genome Res* **16**, 123-131 (2006).
10. P. G. Giresi, J. Kim, R. M. McDaniell, V. R. Iyer, J. D. Lieb, FAIRE (Formaldehyde-Assisted Isolation of Regulatory Elements) isolates active regulatory elements from human chromatin. *Genome Res* **17**, 877-885 (2007).
11. J. D. Buenrostro, P. G. Giresi, L. C. Zaba, H. Y. Chang, W. J. Greenleaf, Transposition of native chromatin for fast and sensitive epigenomic profiling of open chromatin, DNA-binding proteins and nucleosome position. *Nat Methods* **10**, 1213-1218 (2013).
12. Z. Lu *et al.*, The prevalence, evolution and chromatin signatures of plant regulatory elements. *Nat. Plants* **5**, 1250-1259 (2019).
13. E. Calo, J. Wysocka, Modification of enhancer chromatin: what, how, and why? *Mol Cell* **49**, 825-837 (2013).
14. M. J. Fullwood, C. L. Wei, E. T. Liu, Y. Ruan, Next-generation DNA sequencing of paired-end tags (PET) for transcriptome and genome analyses. *Genome Res* **19**, 521-532 (2009).
15. E. Lieberman-Aiden *et al.*, Comprehensive mapping of long-range interactions reveals folding principles of the human genome. *Science* **326**, 289-293 (2009).
16. T. Li, L. Jia, Y. Cao, Q. Chen, C. Li, OCEAN-C: mapping hubs of open chromatin interactions across the genome reveals gene regulatory networks. *Genome Biol* **19**, 54 (2018).
17. M. R. Mumbach *et al.*, HiChIP: efficient and sensitive analysis of protein-directed genome architecture. *Nat Methods* **13**, 919-922 (2016).
18. H. Chai *et al.*, ChIATAC is an efficient strategy for multi-omics mapping of 3D epigenomes from low-cell inputs. *Nat. Commun.* **14**, 213 (2023).
19. M. Louwers *et al.*, Tissue- and expression level-specific chromatin looping at

945 maize b1 epialleles. *Plant Cell* **21**, 832-842 (2009).
946 20. L. Zhao *et al.*, Chromatin loops associated with active genes and
947 heterochromatin shape rice genome architecture for transcriptional regulation.
948 *Nat Commun* **10**, 3640 (2019).
949 21. T. Misteli, Beyond the sequence: cellular organization of genome function. *Cell*
950 **128**, 787-800 (2007).
951 22. A. Göndör, R. Ohlsson, Enhancer functions in three dimensions: beyond the flat
952 world perspective. *F1000Res* **7**, (2018).
953 23. A. Salman-Minkov, N. Sabath, I. Mayrose, Whole-genome duplication as a key
954 factor in crop domestication. *Nat. Plants* **2**, 16115 (2016).
955 24. M. Wang *et al.*, Evolutionary dynamics of 3D genome architecture following
956 polyploidization in cotton. *Nat. Plants* **4**, 90-97 (2018).
957 25. L. Concia *et al.*, Wheat chromatin architecture is organized in genome territories
958 and transcription factories. *Genome Biol.* **21**, 104 (2020).
959 26. S. S. Rao *et al.*, A 3D map of the human genome at kilobase resolution reveals
960 principles of chromatin looping. *Cell* **159**, 1665-1680 (2014).
961 27. K. Davie *et al.*, Discovery of transcription factors and regulatory regions driving
962 in vivo tumor development by ATAC-seq and FAIRE-seq open chromatin
963 profiling. *PLoS Genet* **11**, e1004994 (2015).
964 28. J. Yuan *et al.*, Open chromatin interaction maps reveal functional regulatory
965 elements and chromatin architecture variations during wheat evolution. *Genome*
966 *Biol* **23**, 34 (2022).
967 29. T. I. W. G. S. Consortium *et al.*, Shifting the limits in wheat research and
968 breeding using a fully annotated reference genome. *Science* **361**, eaar7191
969 (2018).
970 30. J. Jia *et al.*, Homology-mediated inter-chromosomal interactions in hexaploid
971 wheat lead to specific subgenome territories following polyploidization and
972 introgression. *Genome Biol* **22**, 26 (2021).
973 31. L. Zhao *et al.*, Deciphering the Transcriptional Regulatory Network Governing
974 Starch and Storage Protein Biosynthesis in Wheat for Breeding Improvement.
975 *Adv Sci (Weinh)* **11**, e2401383 (2024).
976 32. L. Zhao *et al.*, Dynamic chromatin regulatory programs during embryogenesis
977 of hexaploid wheat. *Genome Biol.* **24**, 7 (2023).
978 33. M. J. Rowley, V. G. Corces, Organizational principles of 3D genome
979 architecture. *Nat Rev Genet* **19**, 789-800 (2018).
980 34. E. de Wit, E. P. Nora, New insights into genome folding by loop extrusion from
981 inducible degron technologies. *Nat Rev Genet* **24**, 73-85 (2023).
982 35. A. R. Barutcu, P. G. Maass, J. P. Lewandowski, C. L. Weiner, J. L. Rinn, A TAD
983 boundary is preserved upon deletion of the CTCF-rich Firre locus. *Nat Commun*
984 **9**, 1444 (2018).
985 36. Q. Wu, P. Liu, L. Wang, Many facades of CTCF unified by its coding for three-
986 dimensional genome architecture. *J Genet Genomics* **47**, 407-424 (2020).
987 37. I. F. Davidson, J. M. Peters, Genome folding through loop extrusion by SMC
988 complexes. *Nat Rev Mol Cell Biol* **22**, 445-464 (2021).
989 38. M. Zhang, H. Huang, J. Li, Q. Wu, ZNF143 deletion alters enhancer/promoter
990 looping and CTCF/cohesin geometry. *Cell Rep.* **43**, 113663 (2024).
991 39. C. Liu, Y. J. Cheng, J. W. Wang, D. Weigel, Prominent topologically associated
992 domains differentiate global chromatin packing in rice from Arabidopsis. *Nat*
993 *Plants* **3**, 742-748 (2017).
994 40. E. S. Karaaslan *et al.*, Marchantia TCP transcription factor activity correlates

995 with three-dimensional chromatin structure. *Nat Plants* **6**, 1250-1261 (2020).
996 41. Z. Li *et al.*, The bread wheat epigenomic map reveals distinct chromatin
997 architectural and evolutionary features of functional genetic elements. *Genome*
998 *Biol.* **20**, 139 (2019).
999 42. E. Li *et al.*, Long-range interactions between proximal and distal regulatory
1000 regions in maize. *Nat. Commun.* **10**, 2633 (2019).
1001 43. L. Wang *et al.*, Altered chromatin architecture and gene expression during
1002 polyploidization and domestication of soybean. *Plant Cell* **33**, 1430-1446
1003 (2021).
1004 44. L. Deng *et al.*, 3D organization of regulatory elements for transcriptional
1005 regulation in Arabidopsis. *Genome Biol.* **24**, 181 (2023).
1006 45. H. Nordberg *et al.*, The genome portal of the Department of Energy Joint
1007 Genome Institute: 2014 updates. *Nucleic Acids Res* **42**, D26-31 (2014).
1008 46. Y. Liu *et al.*, SorGSD: updating and expanding the sorghum genome science
1009 database with new contents and tools. *Biotechnol Biofuels* **14**, 165 (2021).
1010 47. M. R. Woodhouse *et al.*, A pan-genomic approach to genome databases using
1011 maize as a model system. *BMC Plant Biol.* **21**, 385 (2021).
1012 48. A. Vasudevan, S. Cloutier, Lifting of the 1,000 wheat exome project SNPs from
1013 Triticum aestivum cv. Chinese Spring assembly RefSeq v1.0 to RefSeq v2.1.
1014 *BMC Res. Notes* **16**, 220 (2023).
1015 49. S. K. Muthusamy *et al.*, Genome-Wide Identification and Analysis of Biotic and
1016 Abiotic Stress Regulation of C4 Photosynthetic Pathway Genes in Rice. *Appl.*
1017 *Biochem. Biotechnol.* **187**, 221-238 (2019).
1018 50. C. Hao *et al.*, Resequencing of 145 Landmark Cultivars Reveals Asymmetric
1019 Sub-genome Selection and Strong Founder Genotype Effects on Wheat
1020 Breeding in China. *Mol Plant* **13**, 1733-1751 (2020).
1021 51. F. He *et al.*, Genomic variants affecting homoeologous gene expression dosage
1022 contribute to agronomic trait variation in allopolyploid wheat. *Nat Commun* **13**,
1023 826 (2022).
1024 52. S. Li *et al.*, Genome-wide association study revealed TaHXK3-2A as a
1025 candidate gene controlling stomatal index in wheat seedlings. *Plant Cell*
1026 *Environ* **45**, 2306-2323 (2022).
1027 53. A. Li *et al.*, Wheat breeding history reveals synergistic selection of pleiotropic
1028 genomic sites for plant architecture and grain yield. *Mol Plant* **15**, 504-519
1029 (2022).
1030 54. S. Cheng *et al.*, Harnessing landrace diversity empowers wheat breeding.
1031 *Nature* **632**, 823-831 (2024).
1032 55. J. Qi *et al.*, Mutation of the rice Narrow leaf1 gene, which encodes a novel
1033 protein, affects vein patterning and polar auxin transport. *Plant Physiol* **147**,
1034 1947-1959 (2008).
1035 56. D. Du *et al.*, The TaWAK2-TaNAL1-TaDST pathway regulates leaf width via
1036 cytokinin signaling in wheat. *Sci. Adv.* **10**, eadp5541 (2024).
1037 57. P. Zhao *et al.*, Modern wheat breeding selection synergistically improves above-
1038 and belowground traits. *Plant Physiol.* **196**, 47-50 (2024).
1039 58. R. H. Ramírez-González *et al.*, The transcriptional landscape of polyploid
1040 wheat. *Science* **361**, eaar6089 (2018).
1041 59. R. Stadhouders, G. J. Filion, T. Graf, Transcription factors and 3D genome
1042 conformation in cell-fate decisions. *Nature* **569**, 345-354 (2019).
1043 60. Y. Zhang *et al.*, Transposable elements orchestrate subgenome-convergent and
1044 -divergent transcription in common wheat. *Nat Commun* **13**, 6940 (2022).

61. H. Pei *et al.*, Low-affinity SPL binding sites contribute to subgenome expression divergence in allohexaploid wheat. *Sci. China Life Sci.* **66**, 819-834 (2022).
62. W. Zhang *et al.*, Cytokinin oxidase/dehydrogenase OsCKX11 coordinates source and sink relationship in rice by simultaneous regulation of leaf senescence and grain number. *Plant Biotechnol. J.* **19**, 335-350 (2021).
63. Z. Lu, W. A. Ricci, R. J. Schmitz, X. Zhang, Identification of cis-regulatory elements by chromatin structure. *Curr Opin Plant Biol* **42**, 90-94 (2018).
64. Y. Peng *et al.*, Chromatin interaction maps reveal genetic regulation for quantitative traits in maize. *Nat Commun* **10**, 2632 (2019).
65. D. K. Saini *et al.*, Comprehensive evaluation of mapping complex traits in wheat using genome-wide association studies. *Mol. Breed.* **42**, 1 (2021).
66. J. H. Sahito *et al.*, Advancements and Prospects of Genome-Wide Association Studies (GWAS) in Maize. *Int. J. Mol. Sci.* **25**, 1918 (2024).
67. H. Cui, Challenges and Approaches to Crop Improvement Through C3-to-C4 Engineering. *Front. Plant Sci.* **12**, (2021).
68. B. P. Williams *et al.*, An Untranslated cis-Element Regulates the Accumulation of Multiple C4 Enzymes in Gynandropsis gynandra Mesophyll Cells. *Plant Cell* **28**, 454-465 (2016).
69. I. Reyna-Llorens *et al.*, Ancient duons may underpin spatial patterning of gene expression in C<sub>4</sub> leaves. *Proceedings of the National Academy of Sciences* **115**, 1931-1936 (2018).
70. A. R. Borba *et al.*, Compartmentation of photosynthesis gene expression in C4 maize depends on time of day. *Plant Physiol* **193**, 2306-2320 (2023).
71. J. Swift *et al.*, Single nuclei sequencing reveals C<sub>4</sub> photosynthesis is based on rewiring of ancestral cell identity networks. *bioRxiv*, 2023.2010.2026.562893 (2023).
72. D. Xiang *et al.*, The Transcriptional Landscape of Polyploid Wheats and Their Diploid Ancestors during Embryogenesis and Grain Development. *Plant Cell* **31**, 2888-2911 (2019).
73. Y. Xie *et al.*, Transposable element-initiated enhancer-like elements generate the subgenome-biased spike specificity of polyploid wheat. *Nat Commun* **14**, 7465 (2023).
74. Q. Song, T. Zhang, D. M. Stelly, Z. J. Chen, Epigenomic and functional analyses reveal roles of epialleles in the loss of photoperiod sensitivity during domestication of allotetraploid cottons. *Genome Biol.* **18**, 99 (2017).
75. W. A. Whyte *et al.*, Master transcription factors and mediator establish super-enhancers at key cell identity genes. *Cell* **153**, 307-319 (2013).
76. D. M. Emms, S. Kelly, OrthoFinder: solving fundamental biases in whole genome comparisons dramatically improves orthogroup inference accuracy. *Genome Biol* **16**, 157 (2015).
77. Y. Long, J. F. Wendel, X. Zhang, M. Wang, Evolutionary insights into the organization of chromatin structure and landscape of transcriptional regulation in plants. *Trends Plant Sci.* **29**, 638-649 (2024).
78. Y. Liu *et al.*, Epigenomic identification of vernalization cis-regulatory elements in winter wheat. *Genome Biol.* **25**, 200 (2024).
79. B. J. Reinhart, E. G. Weinstein, M. W. Rhoades, B. Bartel, D. P. Bartel, MicroRNAs in plants. *Genes Dev* **16**, 1616-1626 (2002).
80. H. Wang, H. Wang, The miR156/SPL Module, a Regulatory Hub and Versatile Toolbox, Gears up Crops for Enhanced Agronomic Traits. *Mol Plant* **8**, 677-688

(2015).
81. S. Wingett *et al.*, HiCUP: pipeline for mapping and processing Hi-C data. *F1000Res* **4**, 1310 (2015).
82. R. F. McCormick *et al.*, The Sorghum bicolor reference genome: improved assembly, gene annotations, a transcriptome atlas, and signatures of genome organization. *The Plant Journal* **93**, 338-354 (2018).
83. M. B. Hufford *et al.*, De novo assembly, annotation, and comparative analysis of 26 diverse maize genomes. *Science* **373**, 655-662 (2021).
84. Y. Kawahara *et al.*, Improvement of the Oryza sativa Nipponbare reference genome using next generation sequence and optical map data. *Rice (N Y)* **6**, 4 (2013).
85. T. Zhu *et al.*, Optical maps refine the bread wheat Triticum aestivum cv. Chinese Spring genome assembly. *Plant J* **107**, 303-314 (2021).
86. H. Li, R. Durbin, Fast and accurate long-read alignment with Burrows-Wheeler transform. *Bioinformatics* **26**, 589-595 (2010).
87. N. Servant *et al.*, HiC-Pro: an optimized and flexible pipeline for Hi-C data processing. *Genome Biol* **16**, 259 (2015).
88. J. Feng, T. Liu, B. Qin, Y. Zhang, X. S. Liu, Identifying ChIP-seq enrichment using MACS. *Nat Protoc* **7**, 1728-1740 (2012).
89. J. Wolff *et al.*, Galaxy HiCExplorer 3: a web server for reproducible Hi-C, capture Hi-C and single-cell Hi-C data analysis, quality control and visualization. *Nucleic Acids Res.* **48**, W177-W184 (2020).
90. K. C. Akdemir, L. Chin, HiCPlotter integrates genomic data with interaction matrices. *Genome Biol.* **16**, 198 (2015).
91. A. Kechin, U. Boyarskikh, A. Kel, M. Filipenko, cutPrimers: A New Tool for Accurate Cutting of Primers from Reads of Targeted Next Generation Sequencing. *J Comput Biol* **24**, 1138-1143 (2017).
92. A. M. Bolger, M. Lohse, B. Usadel, Trimmomatic: a flexible trimmer for Illumina sequence data. *Bioinformatics* **30**, 2114-2120 (2014).
93. A. Dobin *et al.*, STAR: ultrafast universal RNA-seq aligner. *Bioinformatics* **29**, 15-21 (2013).
94. B. Li, C. N. Dewey, RSEM: accurate transcript quantification from RNA-Seq data with or without a reference genome. *BMC Bioinf.* **12**, 323 (2011).
95. M. D. Robinson, D. J. McCarthy, G. K. Smyth, edgeR: a Bioconductor package for differential expression analysis of digital gene expression data. *Bioinformatics* **26**, 139-140 (2010).
96. D. V. Klopfenstein *et al.*, GOATOOLS: A Python library for Gene Ontology analyses. *Sci Rep* **8**, 10872 (2018).
97. B. Langmead, S. L. Salzberg, Fast gapped-read alignment with Bowtie 2. *Nat Methods* **9**, 357-359 (2012).
98. H. Thorvaldsdóttir, J. T. Robinson, J. P. Mesirov, Integrative Genomics Viewer (IGV): high-performance genomics data visualization and exploration. *Briefings Bioinf.* **14**, 178-192 (2012).
99. A. R. Quinlan, I. M. Hall, BEDTools: a flexible suite of utilities for comparing genomic features. *Bioinformatics* **26**, 841-842 (2010).
100. Y. Chen *et al.*, A Collinearity-Incorporating Homology Inference Strategy for Connecting Emerging Assemblies in the Triticeae Tribe as a Pilot Practice in the Plant Pangenomic Era. *Mol Plant* **13**, 1694-1708 (2020).
101. S. Heinz *et al.*, Simple combinations of lineage-determining transcription factors prime cis-regulatory elements required for macrophage and B cell

identities. *Mol Cell* **38**, 576-589 (2010).
102. T. Wu *et al.*, clusterProfiler 4.0: A universal enrichment tool for interpreting omics data. *Innovation (Camb)* **2**, 100141 (2021).
103. K. J. Livak, T. D. Schmittgen, Analysis of Relative Gene Expression Data Using Real-Time Quantitative PCR and the 2−ΔΔCT Method. *Methods* **25**, 402-408 (2001).
104. B. Zhao, Y. Xi, J. Kim, S. Sung, Chromatin architectural proteins regulate flowering time by precluding gene looping. *Sci Adv* **7**, (2021).
105. W. Li *et al.*, A Novel N-Methyltransferase in Arabidopsis Appears to Feed a Conserved Pathway for Nicotinate Detoxification among Land Plants and Is Associated with Lignin Biosynthesis. *Plant Physiol* **174**, 1492-1504 (2017).
106. A. Zhou, Y. Bu, T. Takano, X. Zhang, S. Liu, Conserved V-ATPase c subunit plays a role in plant growth by influencing V-ATPase-dependent endosomal trafficking. *Plant Biotechnol. J.* **14**, 271-283 (2016).

## Supplemental figures and legends

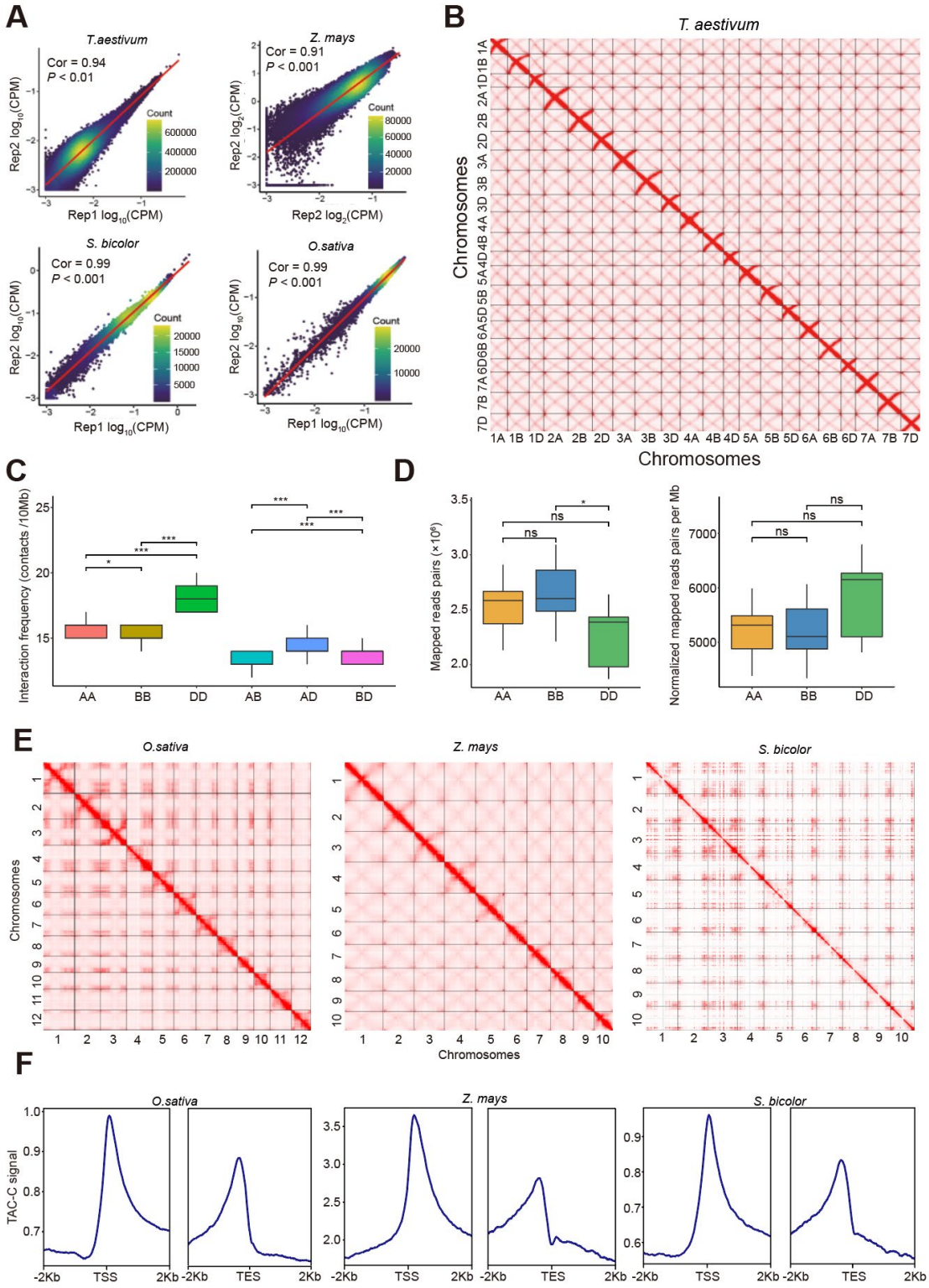


**Fig. S1 Reproducibility, contact matrix and TAC-C signal of TAC-C across four species.**

**A.** Scatter plots showing the reproducibility between two TAC-C replicates of *O. sativa*, *S. bicolor, Z. mays* and *T. aestivum*.

**B.** TAC-C contact matrix of the hexaploid wheat across 21 chromosomes
**C.** The median interaction frequency between 10-Mb bins for each combination of subgenomes between different chromosomes.
**D.** The mapped reads for each combination of subgenomes between same chromosomes (left panel) and normalized by chromosomes length (Mb) (right panel).
**E.** TAC-C contact matrix for *O. sativa*, *Z. mays* and *S. bicolor.*
**F.** TAC-C signal around transcription start site (TSS) and transcription termination site (TTS) for *O. sativa*, *Z. mays* and *S. bicolor.*

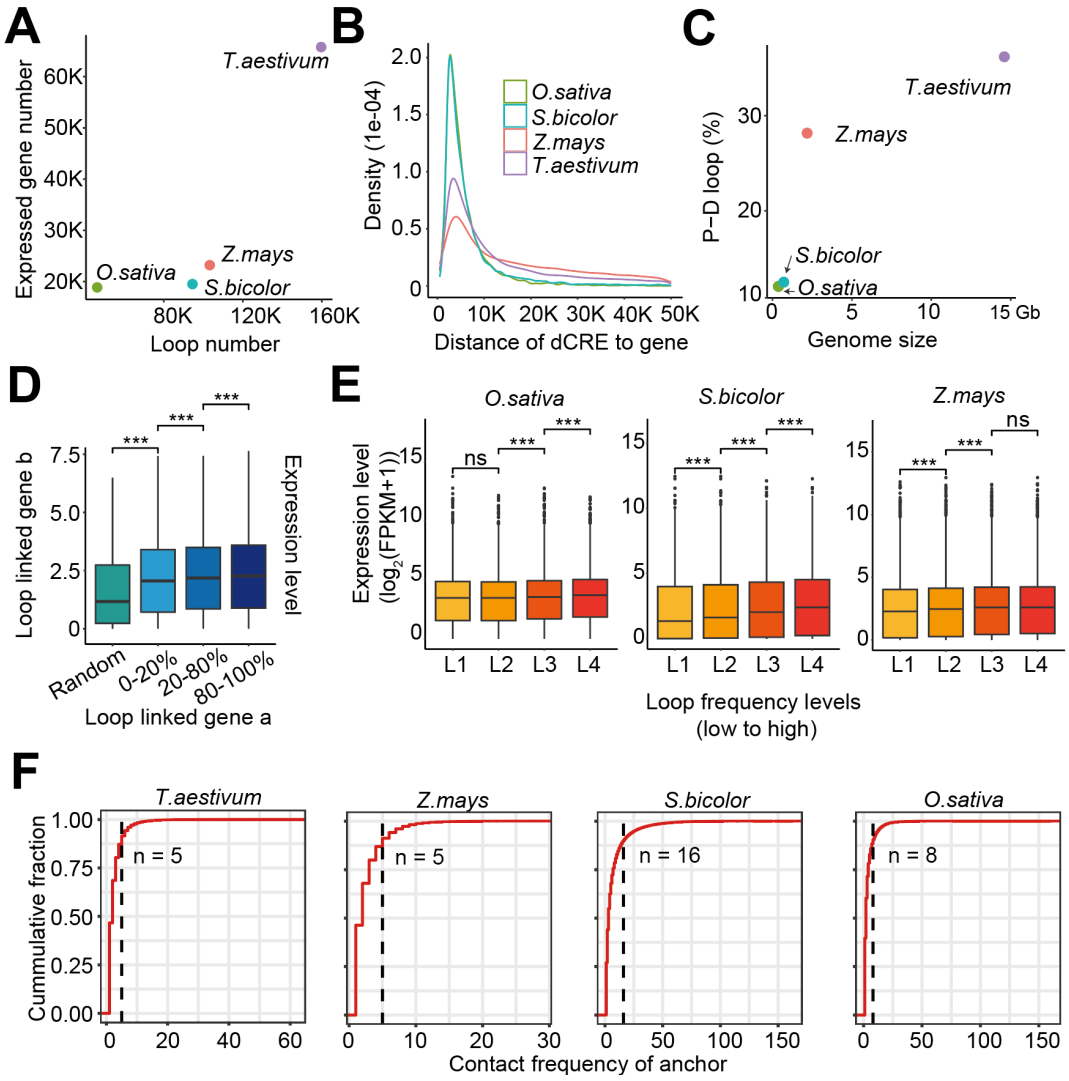


**Fig. S2 Characteristics of chromatin interactions in crop species**

**A.** Correlation between loop counts and expressed gene across the four crop species. Genes with TPM>0.5 were considered expressed.
**B.** Distribution of the distance between dCRE and transcription start site (TSS) of genes across the four crop species.
**C.** Association between the proportion of PDI loop and genome size across the four crop species.
**D.** Contour plot showing log-transformed FPKM values for gene pairs connected by TAC-C loops.
**E.** Expression levels of the loop linked gene pairs. The gene expression levels from

high to low was divided into three categories: 80–100%, 20–80%, and 0–20%. Gene pairs with similar distances were randomly selected as controls. More blue wavy lines indicate higher expression. ***, $p<0.001$, from Student's *t*-test.

**F.** Cumulative fraction of contact frequency for anchors in the four crop species. Dashed lines indicate the threshold, with anchors exceeding the frequency defined as hub anchors.

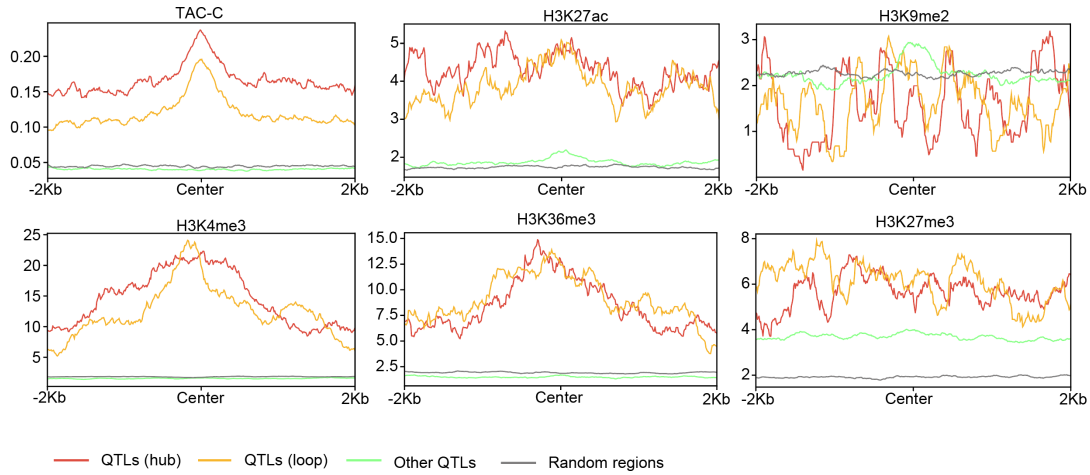


**Fig. S3 Distribution of the TAC-C and representative histone modifications around QTL regions. The center represents the TAC-C peak where the most significant SNP of the QTL is located**

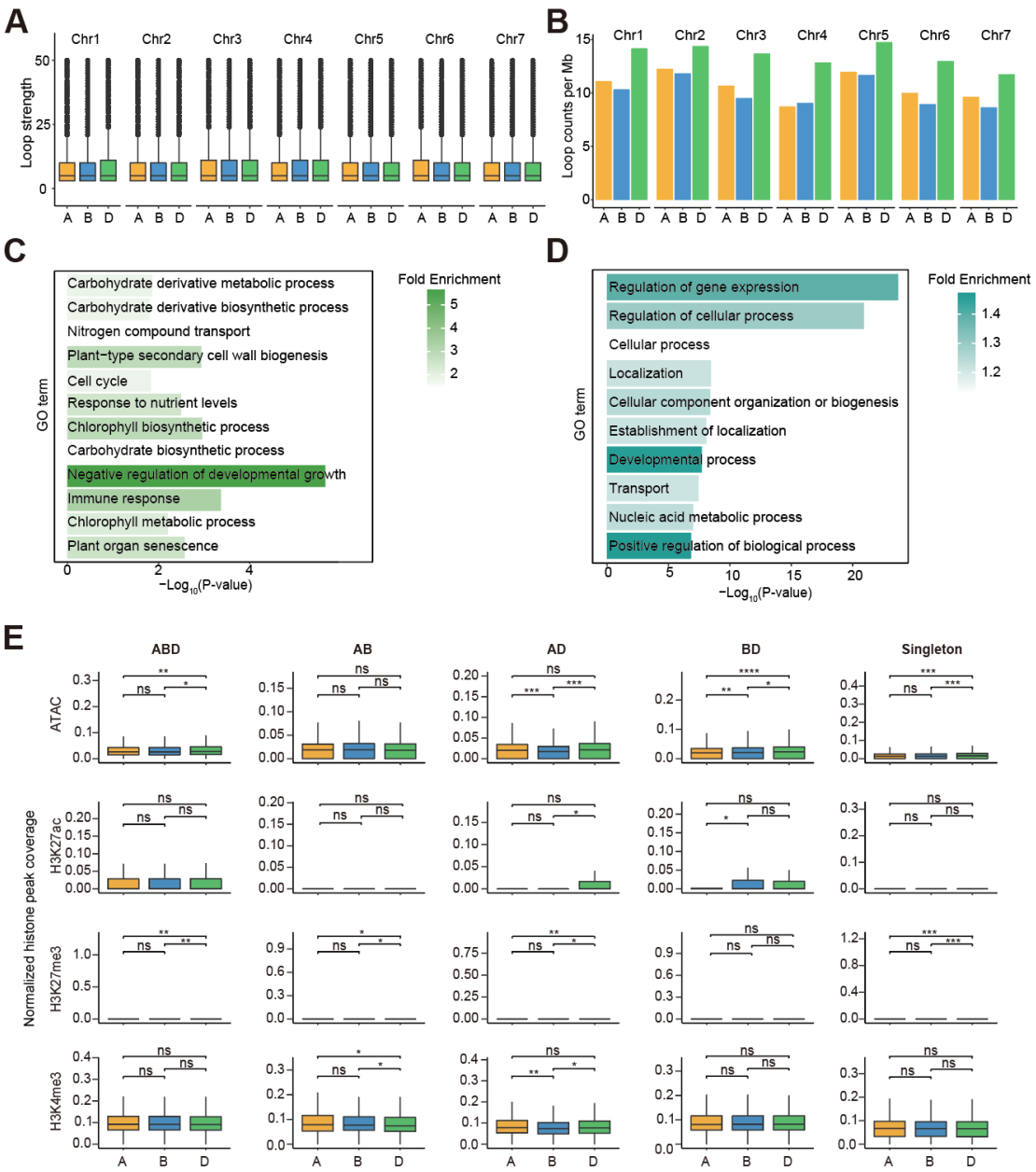


**Fig. S4 Open chromatin loops across the A, B and D subgenomes**

**A.** Boxplot showing loop strength across the 21 wheat chromosomes.
**B.** Loop counts per Mb across the 21 wheat chromosomes.
**C.** GO enrichment analysis of genes linked to ABD homoeolog PPIs.
**D.** GO enrichment analysis of genes linked to singleton PPIs.
**E.** Coverage of ATAC, H3K27ac, H3K27me3, and H3K4me3 peaks in the 5 kb flanking regions of PPI-linked genes at different homoeolog levels in subgenomes A, B, and D. *, $p \leq 0.05$; **, $p \leq 0.01$; ***, $p \leq 0.001$ from Student's *t*-test.

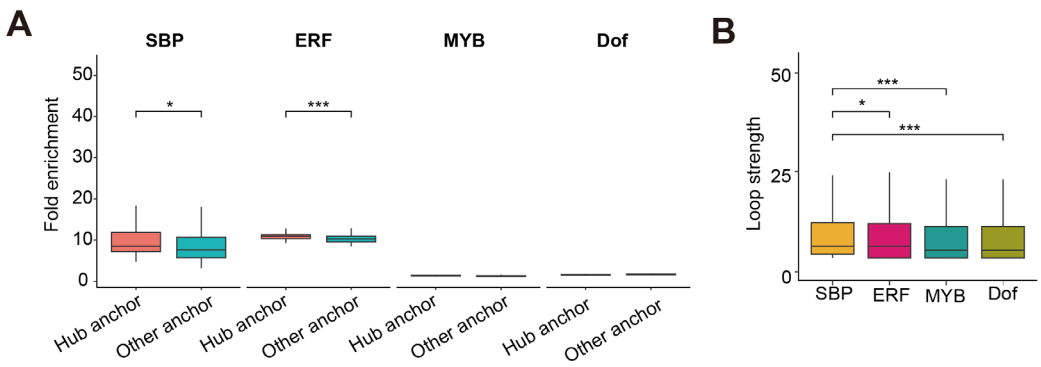


**Fig. S5 Difference in TF-associated chromatin topology.**

**A.** The fold enrichment (compare to random regions) of overlapped interactions between hub anchor, other anchor and random regions with SBP, ERF, MYB and Dof DAP-seq peaks. To minimize false positive errors, the 100 permutation tests were conducted in comparison. In each permutation test, 2000 accessions were randomly sampled from each of the different compared groups. *, $p \leq 0.05$; ***, $p \leq 0.001$ from Student's *t*-test.

**B.** The boxplot shown the strength of loop containing five TF families DAP-seq peak. *, $p \leq 0.05$; ***, $p \leq 0.001$ from Student's *t*-test.

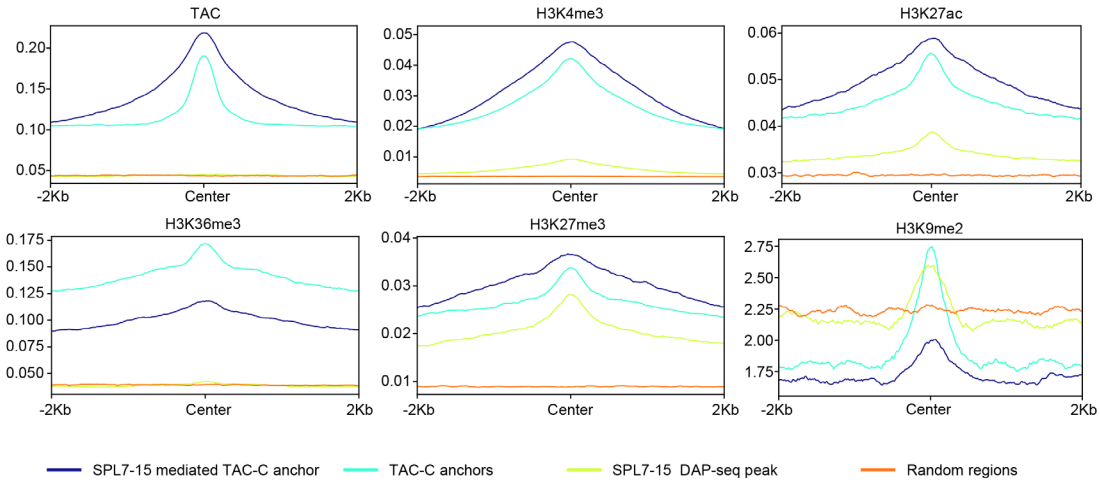


**Fig. S6 Distribution of the TAC-C and representative histone modifications around loop anchor regions.**

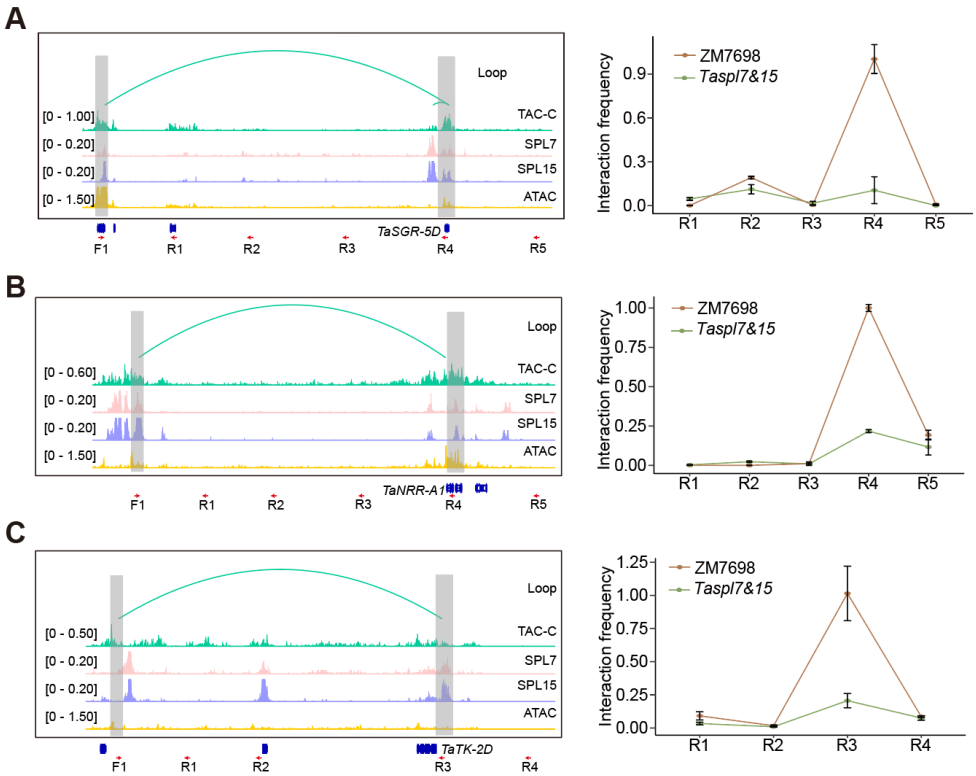


**Fig. S7 Examples of loops lost in *Taspl7&15* compared to ZM7698**

**A-C.** The left panel is the quantitative relative interacting frequency of loop regions determined by 3C-qPCR in ZM7698 and *Taspl7&15*. The right panel is the quantitative relative expression of *TaCKX11-B* by RT-PCR assay in ZM7698 and *Taspl7&15*. Error bars: ±SD.

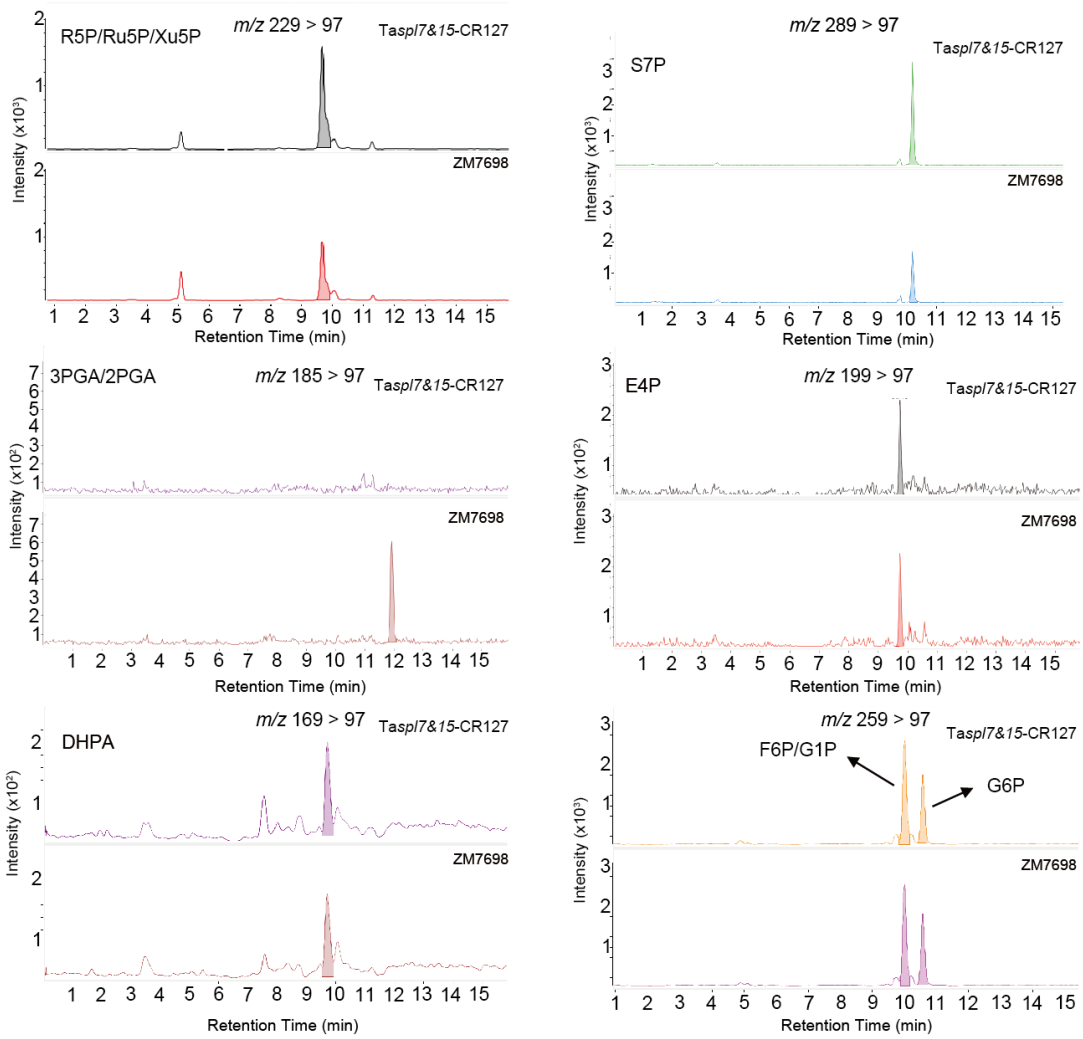


1230

1231 **Fig. S8 LC-QQQ-MS analysis of endogenous R5P/Ru5P/Xu5P, S7P, 3PGA/2PGA,**
1232 **E4P, DHPA, F6P/G1P and G6P from seedlings leaves of ZM7698 and *Taspl7&15*.**

1233

1234 **Supplemental Tables**

1235 Table S1. Summary statistics of TAC-C libraries

1236 Table S2. The intrachromosomal open chromatin loops

1237 Table S3. The functional region used in this study

1238 Table S4. Differentially expressed genes in *Taspl7&15* vs ZM7698

1239 Table S5. Differentially expressed genes related to photosynthetic energy metabolism

1240 Table S6. Chemicals and enzymes used in the TAC-C experiment

1241 Table S7. Primers used in this study